UNIVERSIDADE DE LISBOA
FACULDADE DE CIÊNCIAS
DEPARTAMENTO DE FÍSICA

A multimodal toolbox for dynamic PET and MR data analysis

Ana Margarida Rodrigues Morgado

Mestrado Integrado em Engenharia Biomédica e Biofísica
Perfil em Radiações em Diagnóstico e Terapia

Dissertação orientada por:
Professor Doutor Nuno Matela e Doutora Liliana Caldeira

2016

À memória da minha avó

Resumo

A imagiologia é a especialidade médica que permite a obtenção, de forma não invasiva, de imagens de diversos órgãos e sistemas, constituindo uma ferramenta indispensável na Medicina atual. A evolução das técnicas de imagiologia médica, bem como a diversidade de metodologias, têm permitido evidentes melhorias no diagnóstico e planeamento cirúrgico e terapêutico, para além da sua contribuição para a compreensão do corpo humano.

Atualmente, as técnicas de medicina nuclear, das quais se destaca a tomografia por emissão de positrões (PET, acrónimo inglês de *positron emission tomography*), são as que apresentam maior especificidade e sensibilidade ao nível molecular, proporcionando a avaliação funcional e metabólica detalhada dos tecidos biológicos. Sendo uma técnica de imagiologia fundamentalmente dirigida para a obtenção de informação fisiológica de processos *in vivo*, através da marcação de moléculas biológicas intervenientes em determinados processos metabólicos com isótopos radioativos, apresenta limitações quanto à disponibilização de informação anatómica. Neste sentido, surgiu a necessidade de combinar as valências que a técnica de PET apresenta com outras modalidade de imagiologia que permitem um elevado detalhe anatómico, ou morfológico, como é o caso das imagens obtidas por tomografia computorizada (CT, acrónimo inglês de *computed tomography*) ou por ressonância magnética (MRI, acrónimo inglês de *magnetic resonance imaging*). Esta foi a razão que conduziu ao desenvolvimento de sistemas híbridos de imagiologia. Os sistemas de PET-CT foram os primeiros exemplares deste tipo de sistemas a serem desenvolvidos e introduzidos em prática clínica. Mais recentemente foram desenvolvidos os sistemas de PET-MRI, os quais vieram colmatar algumas limitações dos sistemas mencionados anteriormente. O facto de as técnicas de CT terem por base a utilização de radiação ionizante, assim como o reduzido contraste entre tecidos moles que as suas imagens apresentam, são algumas das desvantagens desta modalidade de imagem que impulsionaram a sua substituição pela técnica de MRI. Por sua vez, esta modalidade oferece imagens com elevado detalhe anatómico e, adicionalmente, permite a obtenção de informação funcional e estrutural, acrescentando valor às imagens moleculares de PET. De modo a permitir a fusão entre os sistemas de PET e de MRI, foi necessário o desenvolvimento de eletrónica não sensível a campos magnéticos, nomeadamente a

utilização de fotodíodos de avalanche (APDs, acrónimo inglês de *avalanche photodiodes*), em oposição aos detetores convencionais.

O *scanner* BrainPET foi o primeiro sistema de PET que permitiu a aquisição simultânea de imagens cerebrais de PET e de MRI. O sistema 3T MR-BrainPET instalado em Jülich (Forschungszentrum Jülich), desde 2008, é um dos sistemas de PET-MRI desenvolvidos pela Siemens Medical Solutions. Este resulta da combinação do referido sistema BrainPET com o *scanner* de MRI MAGNETOM Trio de 3 T. A introdução de sistemas híbridos de PET-MRI permitiu, assim, correlacionar temporal e espacialmente os dados adquiridos por PET e por MRI.

A combinação de informação primordialmente anatómica proveniente de MRI com informação molecular de PET permite o estudo detalhado de, por exemplo, tumores cerebrais e de distúrbios neurodegenerativos, como a doença de Alzheimer ou a doença de Parkinson. No caso específico de imagens de tumores cerebrais (de gliomas, por exemplo), as quais foram objeto de estudo no presente trabalho, é comum a utilização de imagens de MRI de contraste dinâmico de suscetibilidade (DSC, acrónimo inglês de *dynamic susceptibility contrast*) que permitem a medição dos níveis de perfusão cerebral. Este tipo de modalidade de imagem de MRI requer a injeção de um agente de contraste paramagnético e a rápida aquisição do sinal de MRI durante a sua passagem pelos tecidos. Relativamente à aquisição de dados de PET, é comum a aplicação do radio-traçador [^{18}F]-FET (O-(2-[^{18}F]fluoroethyl)-L-tyrosine), o qual pertence ao grupo dos aminoácidos radioativamente marcados, neste caso, pelo isótopo ^{18}F. Este radio-traçador de PET apresenta uma elevada distribuição da sua concentração nas regiões dos tumores, ao passo que a sua distribuição por células inflamatórias e no restante córtex cerebral é relativamente baixa. Deste modo, são alcançadas imagens com elevado contraste entre o tumor e os tecidos circundantes. Além disso, este radio-traçador permite efetuar o diagnóstico diferencial quanto ao grau dos tumores (de baixo grau, ou grau I, a alto grau, ou grau IV).

A análise dinâmica (tetra-dimensional, 4D) de dados de PET e de MRI tem-se tornado cada vez mais relevante nas vertentes clínica e de investigação, em oposição à análise estática de dados. A análise dos dados adquiridos em função do tempo permite a extração de curvas de actividade-tempo (TAC, acrónimo inglês de *time-activity curves*), tratando-se de informação proveniente de imagens de PET, ou curvas de concentração-tempo (TCC, acrónimo inglês de *time-concentration curves*), no caso de

aquisição de MRI em que são utilizados agentes de contraste que realçam determinadas características das imagens. Estas curvas permitem a avaliação da distribuição temporal e espacial, tanto do radio-traçador (no caso de PET) como do agente de contraste (MRI), pois é possível extrair uma curva de cada voxel da imagem (que chegam a ser milhares ou, até mesmo, dezenas de milhares).

Neste trabalho foram realizadas diversas análises de dados provenientes de aquisições simultâneas de PET e de MRI de pacientes com tumores cerebrais (gliomas e meningiomas). As análises foram desenvolvidas com o intuito de extrair, voxel a voxel, diferentes parâmetros das curvas, como, por exemplo, o valor máximo de atividade ou concentração registado por curva, o tempo decorrido desde o instante da injeção do radio-traçador ou do agente de contraste até ser atingido o máximo de distribuição num determinado ponto (TTP, acrónimo inglês de *time to peak*), a área sob a curva (AUC, acrónimo inglês de *area under the curve*) ou o declive das porções ascendentes e/ou descendentes da curva (também designadas em inglês como *wash-in* e *wash-out*, respetivamente). E, assim, gerar imagens paramétricas que traduzem diferentes características dos dados dinâmicos de PET e de MRI. A utilização de imagens paramétricas tem-se verificado extremamente útil em prática clínica, uma vez que permitem a quantificação de determinados parâmetros que são relevantes no auxílio do diagnóstico de tumores. Um dos desafios encontrados no decorrer da análise dos dados de PET e de MRI foi a escolha de uma função matemática que se pudesse ajustar aos dados e que pudesse, assim, traduzir a realidade, facilitando a extração de parâmetros das curvas. Diversos modelos de ajuste a dados de perfusão têm sido propostos por alguns autores, como, por exemplo, a utilização de funções multi-exponenciais. Neste caso, a função de ajuste aos dados escolhida foi a *gamma-variate function*, visto ser a curva que, de acordo com a literatura, mais frequentemente é usada em estudos hemodinâmicos. O ajuste da função aos dados dinâmicos de PET revelou-se especialmente difícil devido à sua natureza ruidosa. Embora tenha sido aplicado um filtro aos dados de PET, o ruído presente nas imagens (que acaba por ser uma das desvantagens que esta modalidade de imagem médica apresenta) não permitiu a obtenção de todos os parâmetros propostos.

Em última análise, pretendia-se, com este projeto, o desenvolvimento de uma ferramenta de análise conjunta de dados dinâmicos de PET e de MRI que permitisse a identificação de diferentes estruturas (*e.g.* tumores) e a geração de imagens paramétricas

capazes de adicionar valor aos diagnósticos propostos pelos clínicos. O objetivo não foi inteiramente cumprido, pelas razões mencionadas anteriormente. Não obstante, os resultados relativos às imagens paramétricas obtidas tanto para PET, como para MRI, mostram as potencialidades deste tipo de análise de dados.

Palavras-chave: sistemas híbridos de imagiologia, PET-MRI, análise dinâmica de dados, imagens paramétricas, tumores cerebrais

Abstract

Medical imaging techniques available in clinical practice provide important diagnostic information. The introduction of hybrid MR-PET scanners offers new perspectives to better correlate data from MR and PET with respect to the time and space domain. Here, each modality may provide different information for the clinicians.

The aim of this project was to develop an image analysis tool that can be used to help identify different structures (*e.g.* vessels, tumour, non-tumour) from MR-PET data, as well as generate parametric images from different features extracted from dynamic data. For this purpose, dynamic [^{18}F]-FET-PET data and dynamic susceptibility contrast (DSC)-MRI acquired based on EPI sequence were analysed. These dynamic data acquired from brain tumour patients are very useful in tumour assessment, as they provide functional information from the FET data and measurements of perfusion levels from the DSC-MRI, besides other anatomical information from MR data. For the dynamic analysis, motion correction was applied prior to image co-registration. Features from both PET and MR data were extracted, using Matlab, in order to produce parametric images of peak, time to peak (TTP), area under the curve (AUC) and wash-in.

The parametric images obtained from the dynamic PET and MR show a good spatial registration, however the patterns are different. Furthermore, in the FET-PET parametric images an uptake area can be identified in the tumour region. One of the challenges found while doing a voxel-by-voxel analysis is the fitting of the contrast-time curves. For the EPI curves, a good fit of the observed data was achieved. However, for the FET concentration curves, no fitting was able to be applied to all image voxels. The main reason for these findings was due to the noisy nature of FET curves. The correct fitting of the data is important, as the extraction of the features can be affected by the function that is adjusted to the contrast-time curves.

Keywords: hybrid medical imaging, MR-PET, dynamic data analysis, parametric images, brain tumours.

Contents

List of Figures

1. Introduction

Nowadays, a wide variety of non-invasive medical imaging techniques is available. For instance, positron emission tomography (PET) is a nuclear medicine imaging technique which allows quantitative imaging of biochemical and physiological processes *in vivo*. While PET provides detailed information on metabolic processes, complementary anatomical information is often required. In order to accomplish this need, computed tomography (CT) and magnetic resonance imaging (MRI) are two of the most commonly used imaging modalities.

The combination of anatomical and functional information is recurrent, which is why hybrid imaging systems have been developed. The fusion of CT with PET systems was firstly introduced. However, besides the use of ionising radiation (in CT acquisitions), a drawback of PET-CT systems is the limited soft tissue contrast of CT images. An attractive alternative to CT is MRI, which offers many advantages in clinical and preclinical research. Moreover, MRI allows different applications in addition to various anatomical contrasts, such as functional MRI (fMRI), perfusion and diffusion imaging. The integration of MR-PET systems is though more challenging than the PET-CT ones, due to mutual interferences of both systems. The major modification is the use of MR compatible PET detectors, avalanche photodiodes (APDs), instead of the conventional photomultiplier detectors.

The 3T MR-BrainPET scanner developed by Siemens Medical Solutions and installed in Jülich (since 2008) was the first hybrid system for human applications capable of simultaneous MR-PET measurements of the human brain. By combining versatile MR and PET imaging the BrainPET system allows a very detailed analysis of brain tumours, for instance. In case of brain tumour patients, dynamic susceptibility contrast (DSC)-MRI is often used to measure perfusion levels of the brain, while dynamic [^{18}F]-FET PET provides additional functional information on tumour biology. The dynamic analysis of data is becoming more relevant, rather than the analysis of

static data, and with this the extraction of parametric images. In this context, the aim of this work is to develop an image analysis tool that can be used to help identify different structures (*e.g.* vessels, tumour, non-tumour) from MR-PET data, as well as generate parametric images from different features extracted from the dynamic data, exploring the profits of comparing dynamic MR-PET data and its usage in improving diagnostic information.

A general outline of the thesis is presented hereafter. Chapter 2 provides an overview of the basic principles of PET and MRI, and a brief introduction on hybrid MR-PET systems. Also in this chapter, an introduction on dynamic imaging is included. Chapter 3 describes the methodologies concerning the elaborated analyses and chapter 4 presents the results and the corresponding discussion. Finally, chapter 5 presents a general discussion of the achieved results and findings and some alternative strategies for possible similar future works. It also contains a summary of the main conclusions of this work.

2. Literature Review

2.1. Basic Principles of Positron Emission Tomography

Positron emission tomography (PET) is a nuclear medicine imaging technique which uses radioactively labelled metabolic molecules to visually assess and quantitatively measure biochemical and physiological processes *in vivo*. A fundamental principle is used in nuclear medicine, the so-called tracer principle. Introduced in the early 1900s by George de Hevesy, the tracer principle states that radioactive compounds have identical chemical properties and, therefore, participate in metabolic functions in the same way as nonradioactive materials [1]. Because radioactive materials can be detected by way of their emission of gamma rays, substances that take part in metabolic functions are labelled with radionuclides and therefore used to track their flow and distribution in the body. For instance, the positron emitter ^{18}F can be used to label deoxyglucose as fluorodeoxyglucose (^{18}F-FDG). This radiotracer enters the cells the same way as glucose, but its metabolites remain trapped within the cells. Hence, the concentration of the radioactive metabolite grows with time in proportion to the cell's glucose metabolic rate. In this way, the radionuclide decays and emits gamma photons which are recorded by a detector, providing information about the radiotracer's spatial and temporal distribution within the body [2].

2.1.1. Physical Principles

2.1.1.1. Radioactive Decay

Radioactive decay is the process by which an unstable or metastable nucleus transforms into a more stable configuration of protons and neutrons releasing energy by the emission of particles and/or radiation. In this process mass is converted into energy according to Einstein's mass-energy equivalence. The sum of rest masses of particles

involved is reduced after the decay. The transition energy, *i.e.* the energy-equivalent of the difference in rest mass, is mostly transferred as kinetic energy to the emitted particles or is converted into photons [3].

Spontaneous radioactive decay is a quantum mechanical phenomenon. It can be described statistically by the transition probability of an unstable nucleus to a more stable one per unit time [2]. For a sample of a specific radionuclide containing N radioactive nuclei, the average decay rate or activity A is given by

$$A = \frac{dN}{dt} = -\lambda N \tag{2.1}$$

where λ denotes the decay constant specific for each radionuclide. The rate at which nuclei undergo radioactive decay takes the form of an exponential function and is characterised by a well-defined parameter called the half-life $T_{1/2}$

$$N(t) = N(0)e^{-\lambda t} \tag{2.2}$$

$$A(t) = A(0)e^{-\lambda t}, \tag{2.3}$$

with $\lambda = \ln 2/T_{1/2}$. The half-life is a time constant specific for each radionuclide that defines the period of time during which half of the atoms of a sample undergo radioactive decay [4]. The half-lives of relevant PET isotopes are presented in Table 2.1.

Different radioactive decay modes (α-, β- and γ-decay) are known and each radionuclide has its own characteristic properties regarding the transition energy, the type of particles emitted and the average lifetime. In PET, positron emission results from a β^+-decay, in which a proton in the nucleus is converted into a neutron. The decay products are a positron and a neutrino.

Table 2.1. Properties of commonly used PET radionuclides [3].

Nuclide	Half-life $T_{1/2}$ (min)	Max. positron energy (MeV)	Mean positron range in water (mm)
^{11}C	20.4	0.959	1.1
^{13}N	9.96	1.197	1.5
^{15}O	2.03	1.738	2.5
^{18}F	109.8	0.633	0.6

2.1.1.2. Interaction of Positrons with Matter

After emission from the nucleus, the positron interacts with the surrounding matter, losing kinetic energy. The interaction of positrons with matter depends on their kinetic energy. Positrons may interact with nuclei or atomic electrons in elastic collisions, with deflection of the positron and conservation of kinetic energy and linear momentum. Elastic collisions are not important for charged-particle energy loss and detection [5]. In contrast, larger fractions of the proton's kinetic energy are transferred to the shell electrons of surrounding atoms during inelastic collisions. As a result, the atom is ionised or excited. Also, inelastic scattering with nuclei may occur, with positron deflection and loss of its kinetic energy by emitting electromagnetic radiation, the so-called Bremsstrahlung (*i.e.* braking radiation). Bremsstrahlung does not play a dominant role for standard positron emitters applied in PET. When nearly at rest, the positron combines with an electron, with subsequent annihilation, resulting in two 511 keV photons (the rest-mass equivalent of each particle) emitted in opposite directions (180°) to conserve momentum (Figure 2.1).

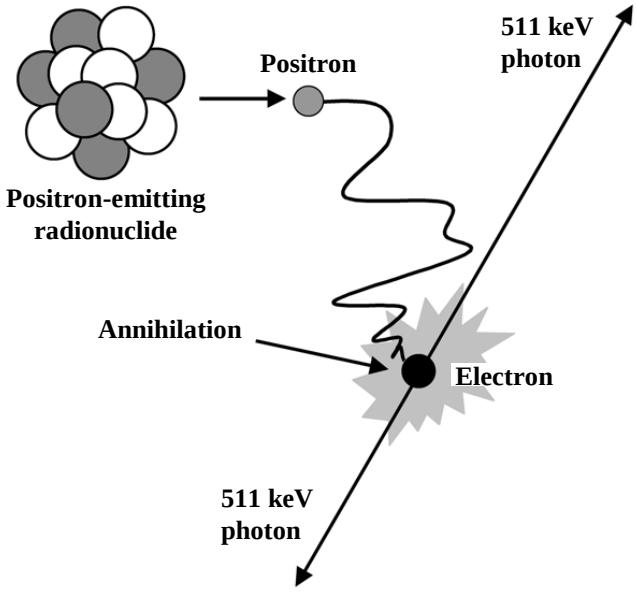

Figure 2.1. Positron emission and subsequent annihilation resulting in two 511 keV annihilation photons with opposite directions. Adapted from [6].

2.1.1.3. Interaction of Photons with Matter

Photons are neutral particles with zero rest-mass, which allows them to travel long distances without interacting with the surrounding medium. Photons coming from the subject under examination are detected by the interactions with the detector material, such as the scintillation crystals. In case of the 511 keV annihilation photons, there are two main mechanisms of interaction with matter relevant for PET: the photoelectric effect and the Compton scattering. The photoelectric effect describes an interaction between a photon and a bound atomic electron (from an inner shell), leading to the ejection of the electron from the atom (Figure 2.2). As a result of the interaction, the photon is absorbed and its energy is transferred to the electron. The kinetic energy of the free electron corresponds to the difference between the photon's energy and the electron's binding energy.

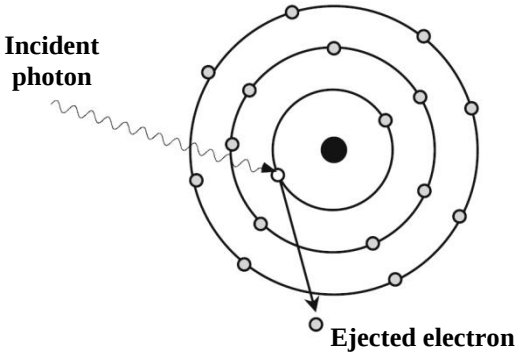

Figure 2.2. Photoelectric effect. Adapted from [3].

Compton scattering is the interaction between a photon and a loosely-bound electron (inelastic collision). The energy of the photon is partly transferred to the electron, which is ejected from the atom, and the photon undergoes a change in direction and energy (Figure 2.3).

In both interactions the absorption process creates an energetic electron that is able to move through the crystal and interact with other atomic electrons, which in the end leads to the production of scintillation light.

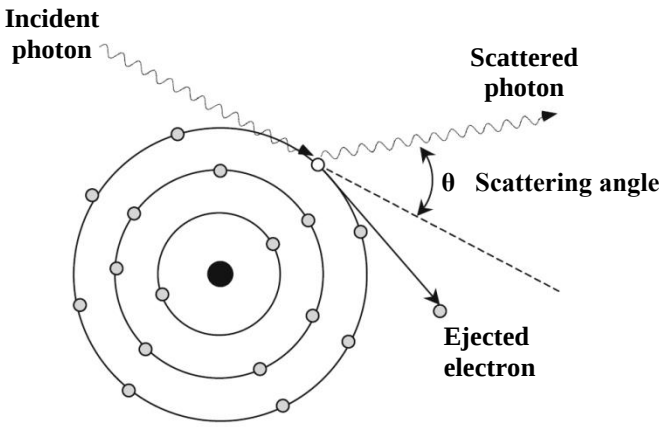

Figure 2.3. Compton scattering. Adapted from [3].

In case of lower energy photons (< 100 keV), the dominant interaction is the photoelectric effect for materials with lower atomic number, *e.g.* body tissues ($Z \lesssim 20$) [4]. For energies between 100 keV and ~10 MeV the dominant effect is Compton scattering, as illustrated in Figure 2.4.

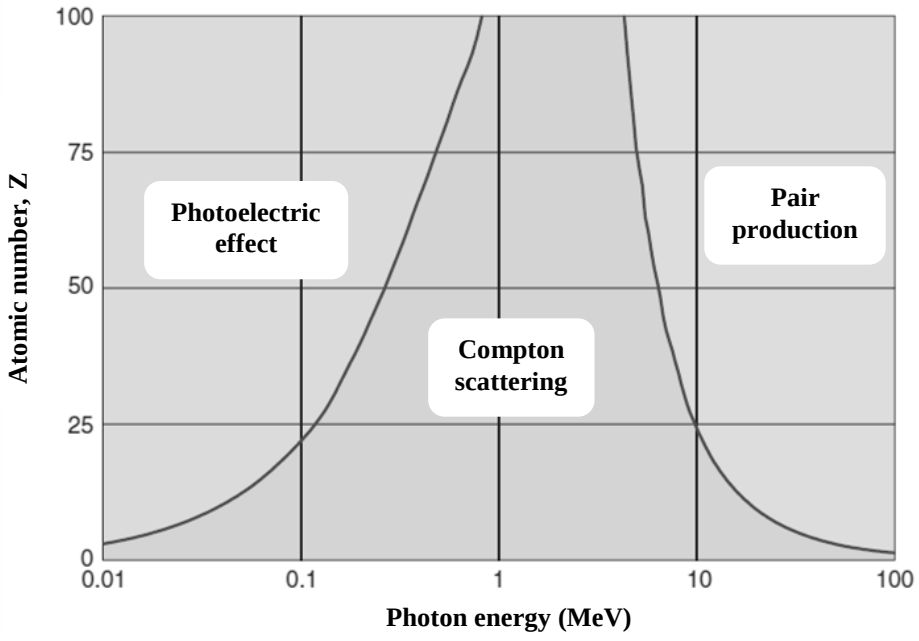

Figure 2.4. Dominating interaction versus photon energy for different atomic numbers [4].

2.1.1.4. Coincidence Detection

PET relies on the detection of pairs of photons originated from annihilation events. The emitted pair of photons defines a line of response (LOR) connecting the positions of the detected photons (Figure 2.5(a)), along which the decay is assumed to have taken place. An event is regarded as valid when the two photons are detected within a defined time interval, called the coincidence time window. Moreover, the energy deposited in the detector by the pair of photons has to be within a selected energy window.

However, some of the registered coincidence events are, in fact, unwanted events, resulting in the assignment of activity to incorrect positions and, consequently, in deterioration of image quality. Thus, true coincidences are only those which derive from single annihilation events and that the pairs of photons reach the detectors, on opposite sides, without interacting significantly with the surrounding matter.

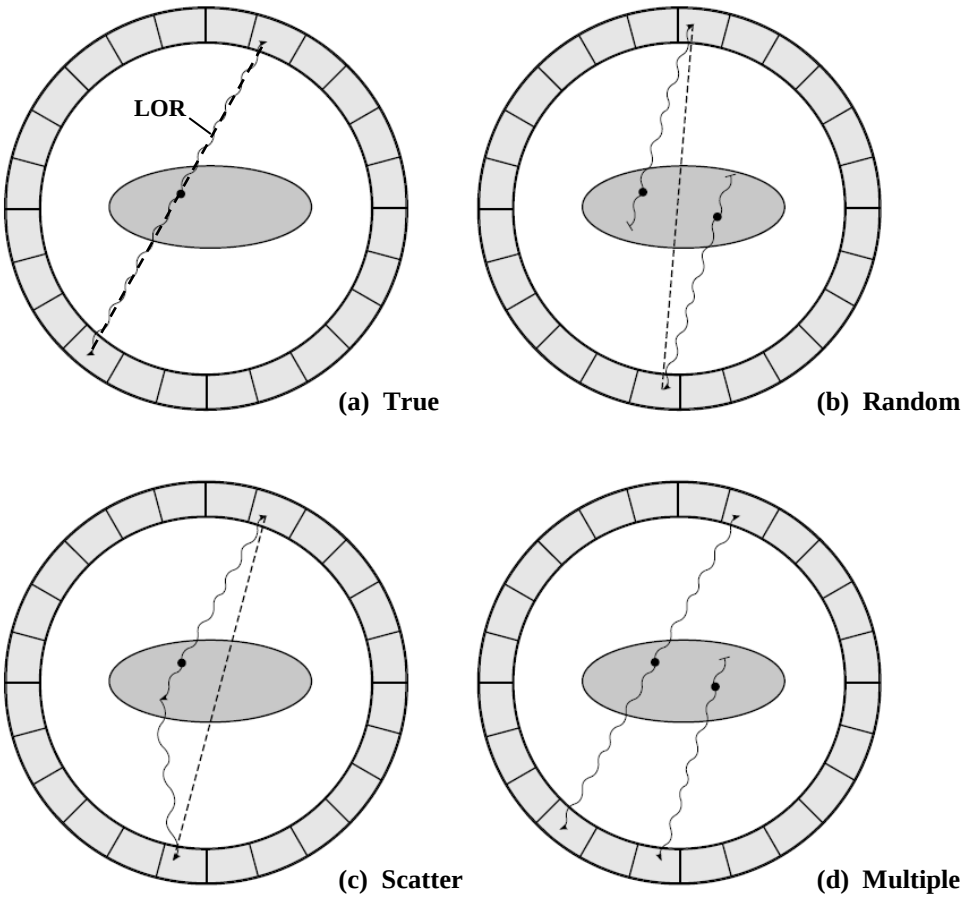

Figure 2.5. Types of coincidence detection. Adapted from [3].

A significant number of photons travelling from the annihilation point towards the detector undergo Compton scattering (Figure 2.5(c)), which is the most probable interaction of the 511 keV annihilation photons, as mentioned in the previous section. Also, random coincidences are detected when photons from unrelated annihilation events occur simultaneously, being counted within the timing window, while their counterparts are lost (Figure 2.5(b)). These events are initially regarded as valid and are assigned to an incorrect LOR. These events lead to an overestimation of the tracer distribution and reduction in image contrast [7]. Finally, multiple coincidences are similar to random events and occur when more than two photons are detected within the coincidence time window (Figure 2.5(d)). In these situations, the ambiguity in deciding which pair of photons arises from the same annihilation event usually leads to the rejection of the events.

2.1.2. Data Corrections

Methodological approaches to correct for various sources of error are required in order to achieve qualitative and quantitative PET data. In this context, corrections can be considered to have their source of error on the interaction of photons with matter, such as scattering, attenuation and random coincidences, or on the characteristics of the scanner, namely normalisation and dead time effects. These are some of the most important corrections required when dealing with PET data and are briefly mentioned hereafter.

2.1.2.1. Compton scattering

Accurate scatter corrections are an important aspect for quantitative PET imaging. Scatter results in decreased image contrast and overestimation of tracer distribution, meaning not only qualitative degradation, but also quantitative inaccuracy.

Since there is a reduction in photon energy after scattering events, energy resolution has to be as good as possible so that only photons with reasonable image information are accepted, *i.e.* only photons exceeding a certain energy threshold are regarded as valid. However, events with small scattering angles can be accepted with this energy discrimination.

Various approaches for estimating and correcting scattered coincidences have been proposed. Scatter can be estimated analytically or numerically. For instance, Monte Carlo simulations are capable of providing accurate results, but are not fast enough to be used in clinical routine. The currently used single scatter simulation (SSS) is a computationally fast 3D algorithm applied in PET scatter correction. This algorithm estimates the expected single scatter coincidence rate considering that only one of the two annihilation photons is scattered. Multiple scatter events are considered less likely to occur. Further information on this topic can be found in [8, 9].

2.1.2.2. Attenuation

As already mentioned, when travelling through the matter, photons interact, mainly by Compton scattering, and lose energy. The attenuation process depends on the transmission length and on the linear attenuation coefficient μ of the medium, which in turn depends on the photon energy [10]. Therefore, two annihilation photons may pass different materials and be attenuated with different probabilities.

Correction factors are needed for each LOR in order to correct images for attenuation. In conventional PET, the correction factors are usually extracted from transmission sources. Attenuation can be directly measured with one or multiple rotating radiation sources (with energies around 511 keV) placed outside the subject.

Alternatively, attenuation correction factors can be extracted from images of the subject acquired with CT or MRI. In case of PET/CT, the CT data represent transmission scans that can be scaled to the right energy of 511 keV. However, the MR images can only be used indirectly, as they represent proton densities, rather than electron densities. Segmentation of MR images and template-based approaches have been developed in this context [11, 12].

2.1.2.3. Random Coincidences

The rate of detected random coincidences is related to the rate of single events on each detector and to the width/length of the timing window. Random coincidences occur homogeneously across the field of view (FOV), adding a homogeneous background that becomes more prominent with increasing count rates. Good temporal resolution is mandatory in order to keep random coincidence rates low.

The delayed time window approach is a commonly used method for random counts correction [2]. This approach includes a normal timing window, during which both true and random coincidences are detected, and a second timing window (the delayed window) measuring random coincidences (Figure 2.6). The probability of detecting a true coincidence in the delayed time window is thus assumed to be null. Since the time windows' width is the same, the rate of random events is estimated to be equal in both windows and the randoms can be subtracted directly from the coincidence data [13].

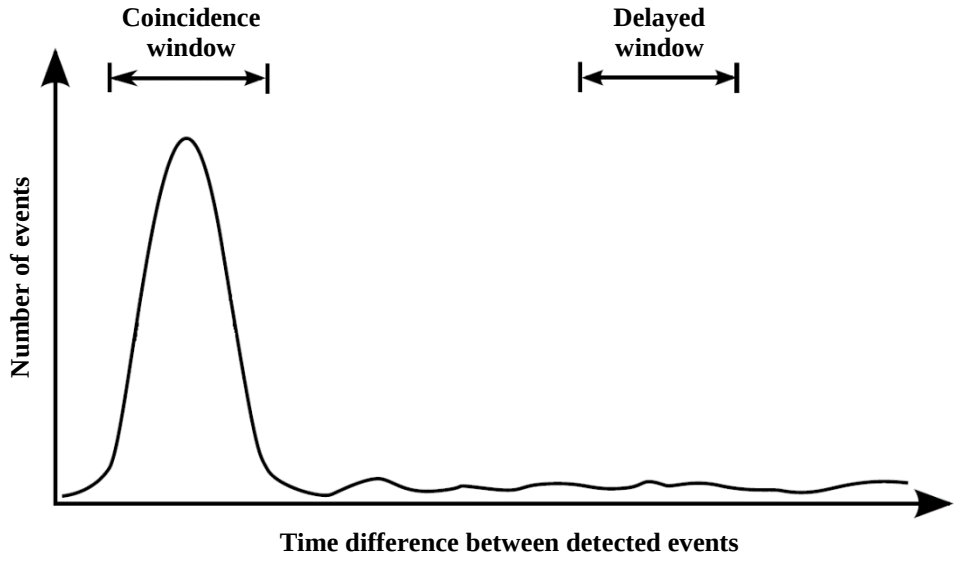

Figure 2.6. Delayed window approach. The coincidence window represents true and random events and the delayed window only random events. Adapted from [2].

2.1.2.4. Normalisation

Normalisation is another process of correction required for the reconstruction of quantitative and artefact-free images. Crystals exhibit varying detection efficiencies, resulting in LORs with inhomogeneous detection efficiencies among the detector. Therefore, individual correction factors for each LOR are required. A plane source measurement is usually performed to acquire the normalisation data. The plane source is placed at the centre of the FOV, which is rotated to a number of different positions [14]. The data from the different views is then merged into a normalisation file, considering only the data from LORs perpendicular to the plane source of every view. This

normalisation file contains the different detector and geometric sensitivities of the scanner [3, 12].

2.1.2.5. Detector Dead Time

The time required by a detector to process an incoming event, during which no further events can be processed, is known as dead time. This causes an underestimation of voxel value of the reconstructed image. With increasing activity, the probability of two or more events occurring within this time period increases.

The dead time effects are significant and additionally can vary within detector blocks among the scanner. Different correction models have been proposed, such as an exponential correction model to describe the dead time of a PET scanner on block level [15, 16]. For the correction of measurement data, parameters for these dead time correction models can be derived from decay experiments [12, 7].

2.1.3. Data Organisation and Image Reconstruction

PET data can be acquired in either 2D or 3D modes. Regarding the temporal information data can also be acquired in different modes, such as the standard list-mode acquisition. With this acquisition mode spatial and temporal information as well as other characteristics of the photon, *e.g.* the energy, are recorded for each detected event. After list-mode acquisition, data is usually stored into sinograms, which can be directly used for image reconstruction. A sinogram for each transaxial place is acquired in 2D data. Each LOR is defined by the distance r of the LOR from the centre of the FOV and the angle of orientation ϕ the LOR (Figure 2.7). The sinogram is thus a 2D histogram of the LORs in the (r, ϕ) Cartesian coordinate system in a given (transaxial) plane. In 3D acquisitions two more variables are needed for the parametrisation of the LORs: the angle θ that defines the angle between the LOR and the transaxial plane and the coordinate z which is the position in the axial direction [17, 3].

There are two basic approaches for the reconstruction of PET images: the analytic and the iterative reconstruction. Analytic reconstruction algorithms require the prior correction of the acquired data. They have the advantage of being computationally fast and straight-forward [2], but have some drawbacks related with the introduction of

blurring in images. The filtered backprojection is the standard analytic reconstruction method applied in PET [2, 6, 3].

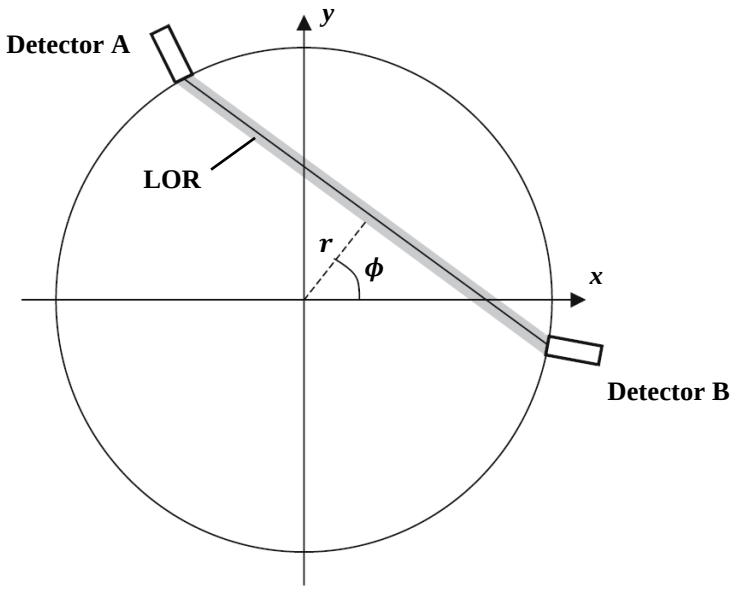

Figure 2.7. Schematic representation of a ring scanner. The sinogram variables $\boldsymbol{r}$ and $\boldsymbol{\phi}$ define the location and orientation of the LOR [3].

Iterative reconstruction is in turn computationally demanding, with longer computation times than analytic methods, but more accurate and realistic in the modelling of imaging process and system response [18]. These methods take into account the statistical properties of the acquired data and noise.

Although there is a variety of iterative reconstruction algorithms, most of them fit a general model structure (Figure 2.8). The iteration begins with an initial estimate of the voxel intensity values of the image, which is forward-projected and compared with the measured data to create a set of projection-space error values. These are then back-projected to the image space in order to obtain image-space error values that are used to update the image estimate. This process is repeated with the new image estimate until some ending criterion is reached [2].

The maximum-likelihood expectation-maximisation (MLEM) algorithm and its variants (*e.g.* the ordered-subset expectation-maximisation (OSEM) algorithm) are the most commonly used iterative reconstruction algorithms in PET [19, 20].

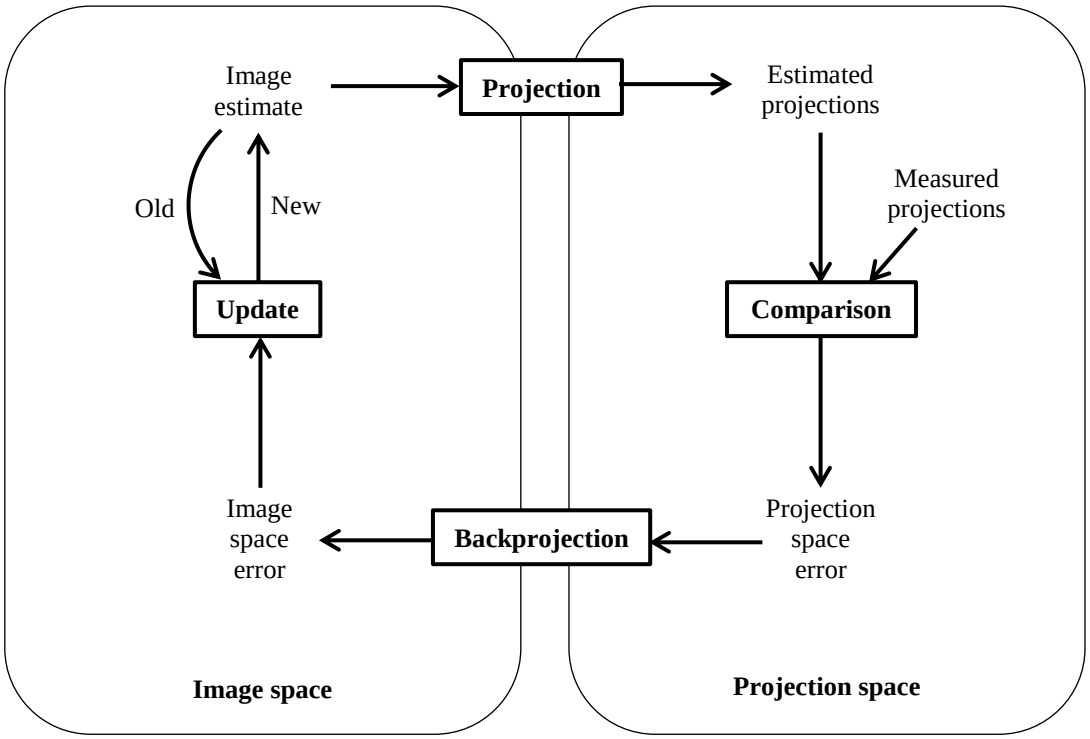

Figure 2.8. Generic model structure of iterative reconstruction algorithms. Adapted from [2].

2.2. Basic Principles of Magnetic Resonance Imaging

Magnetic resonance imaging (MRI) is a medical imaging technique that allows the imaging of anatomical structures with high spatial resolution and soft tissue contrast. Also the delivery of information on perfusion, diffusion and chemical composition of tissue, are such characteristics that make MRI one of the most important imaging modalities in medicine.

For imaging purposes the hydrogen nucleus, containing a single proton, is used due to its abundance in water and fat. However, MRI is not only capable of providing imaging of protons (^{1}H), but also other nuclei less abundant in biological tissues such as sodium (^{23}Na) and phosphorus (^{31}P) [21].

When compared to CT imaging, MRI provides better soft tissue contrast and at the same time avoids the use of ionizing radiation.

2.2.1. Physical Principles

2.2.1.1. Spin and Nuclear Magnetic Resonance

Atomic nuclei with an odd number of protons and/or neutrons possess spin angular momentum, which give rise to the quantum mechanical property of nuclear magnetic resonance (NMR).

Protons possess spin, an intrinsic property of almost all elementary particles. Besides having angular momentum, the proton has magnetic momentum and behaves like a small magnet, which means it is influenced by external magnetic fields and electromagnetic waves. In the presence of an external magnetic field B_0, the spins magnetic moment $\vec{\mu}$ tend to align in the direction of B_0, assumed as the z-direction or longitudinal direction. Also, nuclear spins undergo precession (Figure 2.9) at a well-defined frequency called the Larmor frequency ω. This frequency is related to the strength of the applied magnetic field by the expression

$$\omega = \gamma B_0 \tag{2.4}$$

where the gyromagnetic ratio γ is a known constant that depends on the type of nucleus.

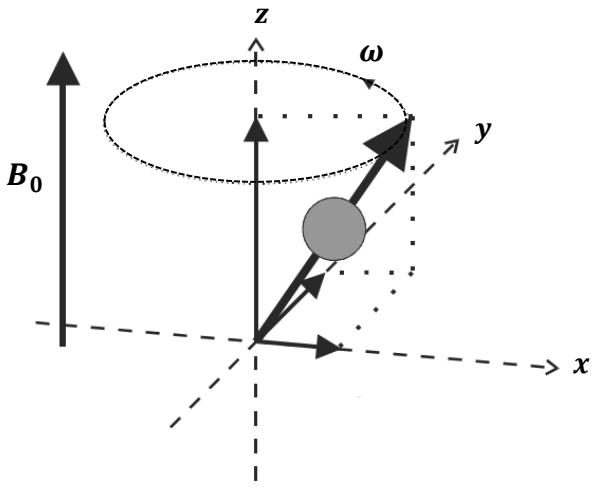

Figure 2.9. External magnetic field ($\boldsymbol{B_0}$) effect on a proton. The proton precesses about the magnetic field, with its precessional axis parallel to $\boldsymbol{B_0}$ [22].

Most whole-body human imaging systems use magnetic fields of $1.5\,T$ and $3\,T$ in clinical practice, and $7\,T$ up to $9.4\,T$ in clinical and preclinical research [7].

While the spin-system reaches a stable state, a net magnetisation vector $\vec{M}$ is set along the patient axis (*z*-axis) as a result of the sum of all the individual magnetic moments. The magnetisation vector has its major contribution in the direction of B_0, which corresponds to the longitudinal magnetisation M_z.

To obtain an MR signal, a radio frequency (RF) pulse is oriented perpendicular to B_0 and tuned to the resonant frequency (ω) of the spins. The RF pulse is produced by a transmission coil placed close to the imaging volume. This manipulation of the magnetisation in the transverse (*xy*) plane excites the spins out of equilibrium and forces them to rotate in phase, increasing the transverse magnetisation M_{xy}. The angle by which the net magnetisation is rotated away from the main magnetic field direction (*z*-axis) is known as the flip angle α [23].

2.2.1.2. Relaxation

After excitation, the return of the net magnetisation vector $\vec{M}$ back to its thermal equilibrium state is observed. The term relaxation describes this phenomenon and is well defined by the relaxation time constants T_1 and T_2. The spin-lattice interaction refers to the T_1 relaxation (or longitudinal relaxation) and characterises the return of $\vec{M}$ along the *z*-direction, that is, the M_z recovery after application of the RF pulse (Figure 2.10). For a 90° excitation ($M_z(0) = 0$) this exponential behaviour is described by

$$M_z = M_0(1 - e^{-t/T_1}), \tag{2.5}$$

where M_0 corresponds to the net magnetisation strength (*i.e.* the equilibrium magnetisation). The behaviour of the transverse component of the magnetisation vector is characterised by the spin-spin time constant which is referred to as T_2 or transverse relaxation (Figure 2.10). This process results in the decay of M_{xy} and thus in MR signal loss. Following a 90° excitation ($M_{xy}(0) = M_0$), this process is given by

$$M_{xy} = M_0 e^{-t/T_2}. \tag{2.6}$$

T_1 and T_2 relaxation time constants, along with the proton density p, are important MR parameters which values vary with the tissue under investigation. In practice, static field inhomogeneities and T_2 decay are observed, resulting in a reduced relaxation time constant T_2^*. The loss of MR signal due to T_2^* effects is known as free induction decay (FID).

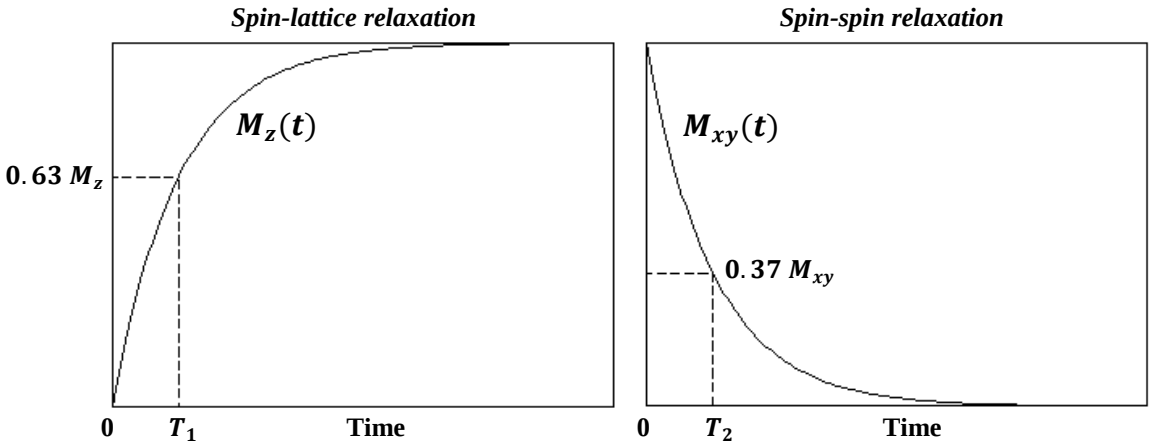

Figure 2.10. Proton relaxation processes: spin-lattice or longitudinal relaxation (left) and spin-spin or transverse relaxation (right).

2.2.1.3. Imaging Principles

When excited, the spins behave like oscillators inducing signals at the Larmor frequency. The total signal (FID signal) generated by all oscillators of the excited area is recorded in a single time waveform, containing no spatial information. So in order to achieve spatial information, linear gradient fields $\vec{G}$ are applied in addition to B_0. These gradient fields can be switched independently in all directions and are therefore denominated as G_x, G_y and G_z. To note that the combined magnetic field (for instance, $B_0 + xG_x$ if a gradient G_x is applied in the *x*-direction) still points in the *z*-direction, only field strength varies. The superposition of gradient fields forces the spins at different locations to precess at different frequencies, thus allowing a selective excitation. Slice selection is consequently achieved as the gradient field is applied within a specific range of frequencies (bandwidth).

Phase- and frequency-encoded data is stored in the Fourier space, or *k*-space, according to the spatial location, and is analysed by the Fourier transform. Image reconstruction can be performed by applying an inverse Fourier transform of the *k*-space.

2.2.2. MRI Sequences

MRI pulse sequences consist of programmed sets of changing RF pulses and magnetic gradients, which are grouped together into an MRI protocol. There are two basic classes of sequences: the spin-echo (SE) pulse sequence and the gradient-echo

(GE) pulse sequence. The SE sequence is the most commonly used in MRI. This pulse sequence can be adjusted to give T_1-weighted, proton density and T_2-weighted images. The term spin-echo refers to the refocusing of precessing spin magnetisation by a 180° pulse at the Larmor frequency (Figure 2.11(a)). The sequence begins with the simultaneous application of a slice selection gradient G_z and a 90° RF excitation pulse. After this, phase- and frequency-encoding gradients, G_y and G_x respectively, are applied. As it is known, the observed MR signal decays with time due to spin-spin relaxation and magnetic field inhomogeneities (T_2^*). The loss of transverse magnetisation can be partly recovered by a 180° refocusing pulse. This pulse is applied at $t = TE/2$ and the so called spin-echo is created at $t = TE$ (Figure 2.11(b)), where the parameter TE refers to the echo time. Because T_2 dephasing is only partly reversible, the maximum of the spin-echo is lower than the maximum signal intensity at $t = 0$. The time between two 90° RF excitations is the repetition time (TR).

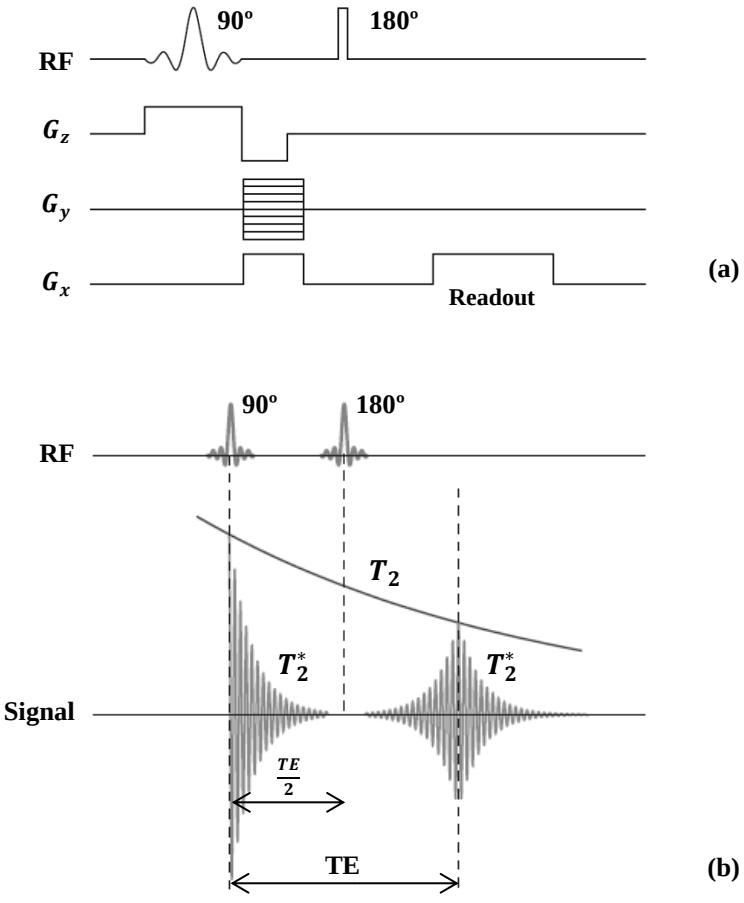

Figure 2.11. Diagram of a spin-echo pulse sequence (a) and corresponding time signal (b) [24].

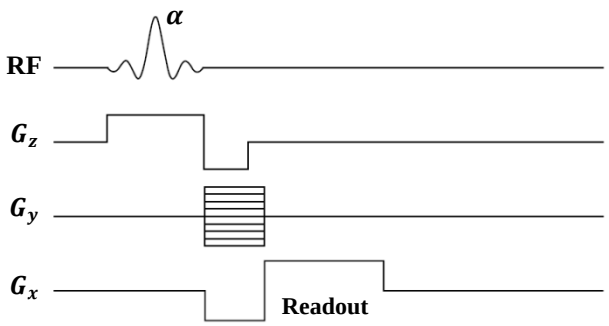

Figure 2.12. Diagram of a gradient-echo pulse sequence [24].

The major drawback of SE sequences is the long imaging times, particularly in proton density and T_2-weighted imaging protocols (as TR is extended to minimize the influence of T_1 relaxation). To overcome this problem GE sequences are used. As compared to SE sequences, they mainly differ in two respects: the application of flip angles that are usually smaller than 90° and the absence of the 180° refocusing pulse (*i.e.* there is no spin-echo). The reduced flip angle leads to a smaller transverse magnetisation, resulting in faster longitudinal magnetisation and, therefore, shorter TR. The rephasing is done by gradient reversal, which implies that the loss of signal results from T_2^* effects. This sequence is thus more sensitive to magnetic field artefacts than SE sequences (Figure 2.12).

An approach to overcome longer MR acquisitions is the development of very fast imaging sequences, such as echo-planar imaging (EPI). EPI is performed using a rapid gradient switching to acquire multiple echoes generated and sampled within the same excitation (Figure 2.13) [25]. A typical matrix size of EPI images is 128×128 and images can be acquired in 20 – 100 ms, allowing a very high temporal resolution. This is of great importance since it allows less motion artefacts and also the ability to image rapid physiologic and kinetic processes of the human body [21, 24]. However, EPI is more sensitive to susceptibility effects and magnetic field inhomogeneities and the obtained signal is more T_2^*-weighted. Concerning the equipment, it requires high performance gradient coils. The EPI sequence is used, for instance, in functional (fMRI), diffusion and perfusion imaging.

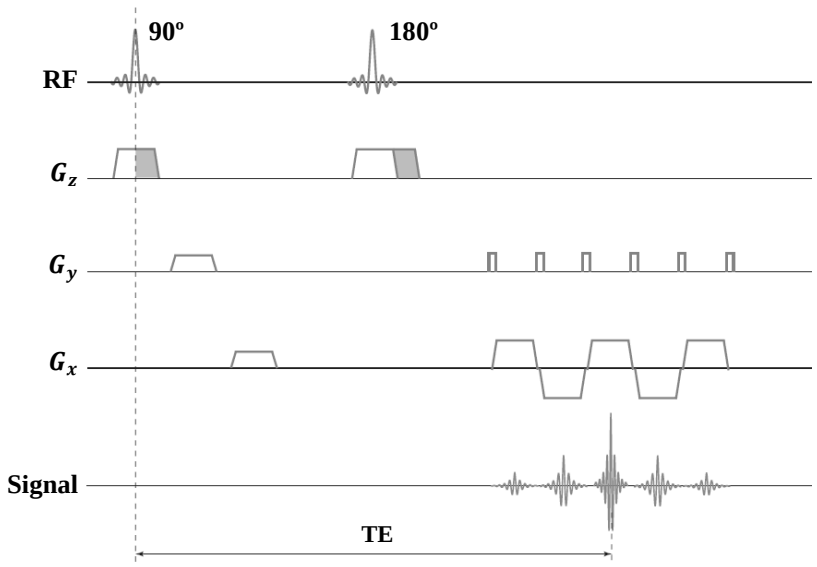

Figure 2.13. Diagram of a T_2-weighted SE EPI sequence [24].

2.3. MR-PET: Hybrid Medical Imaging

In the last few decades, numerous studies have demonstrated an improvement in diagnostic accuracy and better understanding of physiological processes when combining complementary imaging techniques. Whereas CT and MRI are capable of providing mostly anatomical images, nuclear medicine modalities, either PET or single photon emission computed tomography (SPECT), are fundamental to provide functional information.

Multimodal imaging was initially achieved by superimposing images acquired with different scanners. However, the necessity to overcome co-registration errors due to non-simultaneous acquisition became a mandatory condition in the development of hybrid scanners offering bimodal images in a single examination and without repositioning the patient.

The first combined system was a PET/CT, developed in the 1990s [26], which had such a successful impact that stand-alone PET systems quickly disappeared from the market [27, 28]. Nevertheless, MRI exhibits interesting properties making it an appropriate replacement for CT. MRI offers superior soft tissue contrast and spatial resolution and does not use ionising radiation, which otherwise can be a problem in

paediatrics and when repetitive or follow-up studies are required. Furthermore, MRI also possesses different applications in the domain of functional imaging, such as diffusion weighted imaging (DWI) and MR spectroscopy which, moreover, do not rely on the injection of contrast agents [28]. Thus, although PET offers the possibility of studying a wider spectrum of metabolic functions with higher sensitivity, the advantages of whole-body MR-PET are not limited to the complementary imaging of anatomy by MRI and function by PET, but include simultaneous combined functional imaging of each modality.

2.3.1. Advantages and Challenges of Combing PET and MRI

Besides the MRI advantages already mentioned over CT, there are some other benefits from the use of hybrid MR-PET scanners. Even with PET/CT scans, MRI scans are often required for further information, meaning that simultaneous MR-PET measurements increase patient comfort and reduce scan times.

Another advantage of hybrid MR-PET systems is the fact that the acquisition times of MRI and PET do not differ as much as those of CT and PET. This reduced time difference offers the opportunity to really perform simultaneous imaging which might result in qualitatively new ways for investigating functional processes [28]. Also improvements in co-registration of simultaneous MR-PET systems can be derived from the MR images. With the fast acquisition of MR images using the EPI sequence (in the range of seconds), motion parameters can be extracted, allowing thus motion corrected PET and MRI data without external motion tracking [7, 29].

When combining two imaging modalities in a single system there are some technological challenges of possible mutual interferences that have to be overcome. The first obstacle is the incompatibility of the photomultiplier tubes (PMTs) and magnetic fields. Conventional PET systems use PMTs to detect the scintillation light. However, since they are very sensitive to magnetic fields, PMTs cannot be operated inside an MR scanner. As a result, some approaches have been studied in order to overcome this problem, such as the use of optical fibres to guide the scintillation light from the crystals to PMTs placed outside the MR system, or the use of avalanche photodiodes (APDs) and, more recently, silicon photomultipliers (SiPMs) to replace conventional PMTs. Another challenge is the fast switching gradients and the RF fields influence in PET

electronics, which need proper shielding. Also, PET electronics may in turn cause magnetic field inhomogeneities, which have to be compensated by appropriate shimming, and signal-to-noise ratio (SNR) degradation. An additional difficulty in MR-PET scanners, and an active topic of research nowadays, is the attenuation correction, which is a prerequisite for accurate quantitative PET. Unlike the attenuation maps provided by CT, there is no relation between the MR image intensity and the attenuating properties of the tissue (valid for 511 keV photon radiation) [30]. Hence, the attenuation data have to be derived from MR images [31].

2.3.2. MR-BrainPET Scanners

The first hybrid scanner capable of simultaneous MR-PET measurements of the human brain was developed by Siemens Medical Solutions [32], with first study results reported by Schlemmer *et al.* [33].

In the Forschungszentrum Jülich, the installed MR-PET system consists of a BrainPET insert and an MR scanner. The available MR scanners are the Siemens 3T TIM Trio (Figure 2.14(a)) and the 9.4T MR scanner (Figure 2.14(b)). The BrainPET is a first prototype of an MR compatible PET scanner for human imaging developed by Siemens Medical Solution. The combined MR-PET system allows simultaneous imaging, as well as its stand-alone use. Further information on the MR-BrainPET scanner is presented in Chapter 3.

(a) 3T MR-BrainPET **(b) 9.4T MR-BrainPET**

Figure 2.14. MR-BrainPET scanners installed at the Forschungszentrum Jülich: 3T (a) and 9.4T (b).

2.4. Dynamic Imaging

2.4.1. Dynamic PET

Dynamic, or four-dimensional (4D), PET is able to produce parametric images of physiological processes, which often have greater clinical utility than static 3D images [34]. In order to assess these parametric or quantitative biological images, suitable data corrections and reconstruction algorithms (briefly mentioned in previous PET section), as well as accurate biological models are required [18].

Mathematical models (*i.e.* kinetic models) relating the dynamics of the tracer and its biological states to the resultant PET image are used in order to determine the signal of interest. Compartmental models are often used to modulate the tracer kinetics. Each possible tracer's state is considered as a compartment (where tracers are uniformly distributed in space), independent of others and with characteristic volume, concentration and chemical reactions.

Biological models are required in order to define the relation between the measurable time-activity curves (TACs), from PET scans, and the actual physiological parameters that affect the response of the tissue to a delivered radiotracer [35] (Figure 2.15). The amount of tracer in blood, or plasma, is given by the input function, which is necessary to estimate the rate constants in tracer kinetic modelling. The input function can be derived from blood sampling, a population database or from reconstructed images, also known as image derived input functions. The accurate

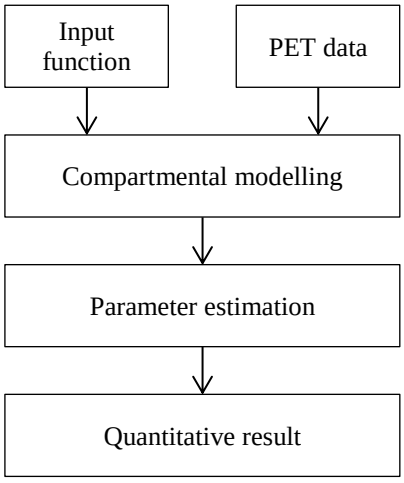

Figure 2.15. Quantitative data analysis steps.

measurement of input function is mandatory to successful quantitative imaging [35]. The kinetic analysis can be processed on a voxel-by-voxel basis, producing parametric images, or on a region of interest (ROI) basis, grouping voxels from homogeneous structures [18]. While a regional analysis allows to process data with better statistics and reduced computing times, as only the average radioactivity of the voxels within a ROI are analysed (instead of thousands of voxels), a voxel-by-voxel analysis is far more complex since the TAC of a single voxel is highly influenced by the noise. Nevertheless, this latter type of analysis might provide better knowledge on the local physiology.

2.4.1.1. Measuring the Amino acid Kinetics

Radiolabelled amino acids have proven to be useful in the diagnostic of brain tumours [36]. The ^{18}F-labelled amino acid O-(2-[^{18}F]fluoroethyl)-L-tyrosine (FET, half-life: 109.8 min) is a PET tracer that shows a strongly increased uptake in cerebral tumours, whereas the uptake in inflammatory cells and the cortex is relatively low, yielding good tumour-to-background contrast [37]. Moreover, the FET uptake enables the discrimination between different tumour grading (low- and high-grade) in both untreated and recurrent gliomas [36, 38].

FET is not incorporated into proteins. Its high uptake in tumour cells is due to the increased transport via the L-system amino acid transporters[1] [39]. Particularly, FET is more selectively transported through LAT2 than through LAT1 (Figure 2.16). As a consequence, this tracer overcomes the limitations of [^{18}F]-FDG by showing higher specificity and, therefore, higher tumour-to-background contrast (Figure 2.17).

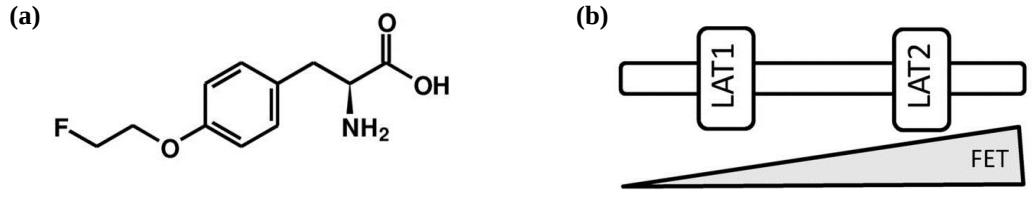

Figure 2.16. Molecular structure of the FET tracer (a) and its selectivity in the L-system amino acid transporters LAT1 and LAT2 (b). Adapted from [38].

[1] L-type amino acid transporters (LATs) are the major transport system for large neutral amino acid, of which subtypes 1 (LAT1) and 2 (LAT2) have been related to the cellular uptake of FET in tumour cells [40, 41].

For all these reasons, FET-PET has gained increasing interest in clinical imaging and, consequently, much information on kinetic analysis have been proposed, but still remains a matter of discussion [36, 42].

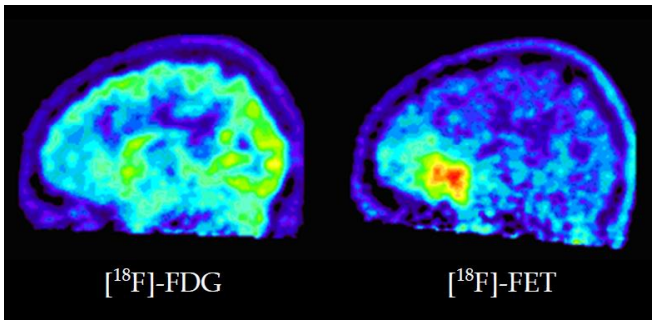

Figure 2.17. [^{18}F]-FDG and [^{18}F]-FET PET contrast images, showing higher tumour-to-background contrast with FET. Adapted from [43].

2.4.2. Dynamic MRI

Dynamic susceptibility contrast (DSC) MRI is the most commonly used method for estimation of perfusion parameters, such as cerebral blood flow (CBF) [44]. Also known as bolus-tracking MRI, DSC-MRI requires the injection of a paramagnetic contrast agent and the fast acquisition of the MR signal loss during its passage through the tissue. The bolus of contrast agent induces a transient signal loss on T_2- and T_2^*-weighted images [45].

DSC-MRI kinetics can be expressed by the convolution expression [46, 44]:

$$C(t) = CBF \cdot AIF(t) \otimes R(t) = CBF \cdot \int_0^t AIF(\tau)R(t-\tau)d\tau \qquad (2.7)$$

where $C(t)$ is the time-dependent concentration of the contrast agent, $AIF(t)$ is the so-called arterial input function (more information can be found in [44]) and $R(t)$ is the impulse response function or residue function, which describes the fraction of contrast agent remaining in the tissue after an instantaneous input bolus.

Although it requires the use of an exogenous contrast agent, DSC-MRI is a very powerful perfusion imaging method due to the wealth of information that can be extracted from the acquired data. Also, its fast acquisition times and use of standard MRI sequences (*e.g.* EPI), as well as good contrast-to-noise ratio, are some of the reasons why DSC-MRI is such a popular and currently the most used brain perfusion imaging method.

2.4.2.1. MRI Contrast Agents

Image contrast in MRI results from differences in signal intensity, which is determined by the properties of the different tissues (intrinsic factors, such as differences in the T_1 and/or T_2 relaxation times) and the properties of the used pulse sequence (extrinsic factors, like the actual sequence or the chosen TR and TE values).

Despite the inherent high contrast of MR images, these signal differences can be further enhanced by the administration of contrast agents (Figure 2.18), which can additionally provide dynamic (pharmacokinetic) information. MRI contrast agents alter the intrinsic contrast properties of biological tissues either by changing the proton density of the tissue or by changing the local magnetic field or the resonance properties of the tissue and, therefore, its T_1 and/or T_2 values [23].

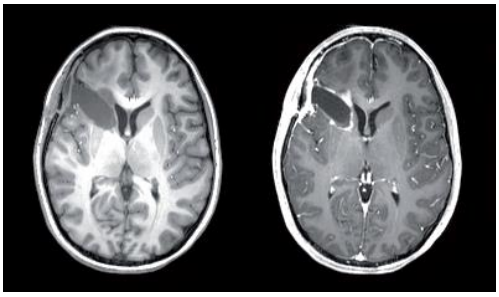

Figure 2.18. T_1-weighted magnetisation-prepared rapid acquisition with gradient echo (MP-RAGE) without contrast medium (left) and T_1-weighted MP-RAGE with contrast medium (right) [47].

Most of clinically available MR contrast media consist of paramagnetic substances, typically gadolinium-based contrast agents [44]. These contrast media substances are mostly toxic metal ions, particularly the gadolinium-based ones, which belongs to the lanthanide series of rare-earth elements. Gadolinium is toxic, in part, by blocking calcium channels, so it must be chelated with an appropriate ligand to allow clinical use [48].

2.4.2.2. Modelling DSC-MRI time-concentration curves

When calculating perfusion parameters it is usual to model time-concentration curves (TCCs) by an analytic function. Given the nature of the contrast bolus, the AIFs and also the tissue concentration curves display a peaked shape, with a baseline period (before the arrival of the bolus), followed by a peak (the first passage of the contrast

agent) and a slower decrease (not returning to baseline values) with a second smaller and wider peak coming afterwards, which is often referred to as the recirculation.

Various functions have been proposed to model the AIFs and, therefore, tissue TCCs. The gamma-variate (GV) function is one of the most commonly used models [44, 49]:

$$y(t) = A(t - t_0)^{\alpha} e^{-(t-t_0)/\beta} \tag{2.8}$$

valid for $t > t_0$, where A is a scaling factor, α and β determine the shape of the curve and t_0 the time at which the bolus arrives at a given region, also referred to as the bolus arrival time (BAT). This function has been often used to describe tracer dilution curves [50, 51, 52]. Thompson *et al.* [50] showed that gamma variates could be fitted to tracer dilution curves with very good agreement.

As previously mentioned, the GV function is generally applied to fit indicator dilution curves, which supported the decision of choosing this method to do the fitting of the analysed data in the current project (which will be discussed hereafter). So, although this subject comes following this modelling section of dynamic MRI, the GV function has similar applications in nuclear medicine [50, 53, 54, 55].

3. Materials and Methods

3.1. The MR-BrainPET Scanner

The clinical data analysed in this work was acquired with the Siemens 3T MR-BrainPET system. As mentioned in Section 2.3, the BrainPET insert was designed to be MR-compatible. For simultaneous MR and PET measurements, the BrainPET is placed inside the bore of the MR scanner (Figure 3.1), with a 36 cm opening for the MR head coil – an adapted head coil with low attenuation for the 511 keV photons [56]. Thus, this configuration minimises attenuation, as well as scatter, as the annihilation photons only need to go through the head coil until reaching the PET detectors.

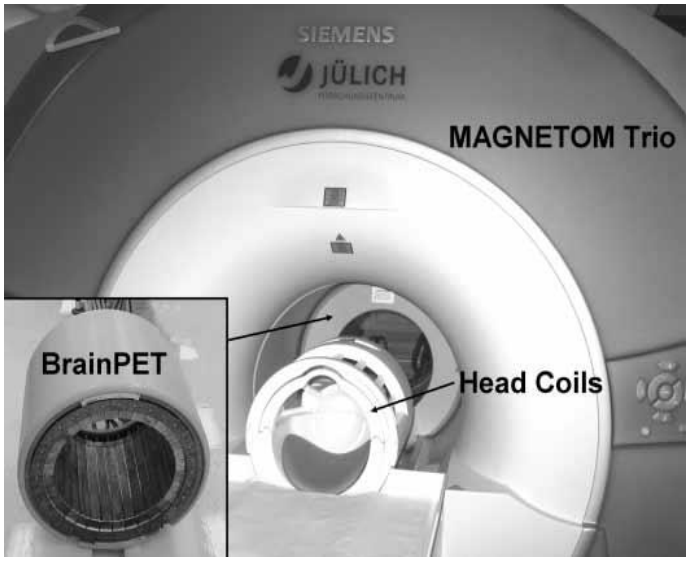

Figure 3.1. The 3T MR-BrainPET installed at the Forschungszentrum Jülich (since 2008). This hybrid scanner consists of a MAGNETOM Trio MRI and the BrainPET insert (placed between the magnet and the MR coils) [27].

3.1.1. BrainPET Component

The BrainPET component consists of 32 copper-shielded detector cassettes, each containing 6 detector blocks with a 12 × 12 LSO[2] crystal matrix (with a crystal size of 2.5 × 2.5 × 20 mm^3 each), placed in a ring. The crystal matrix is read out by a 3 × 3 array of APDs. The signals from the detector cassettes are transmitted via shielded cables of 10 m length and connected to a data acquisition system. The scanner has an axial FOV of about 20 cm and a transaxial FOV of 36 cm (the inner diameter). Further information on the scanner configuration can be found in [28, 12].

3.1.2. Data Acquisition Modes

The data acquisition systems of the two parts of the 3T MR-BrainPET are independent of each other. In particular, the BrainPET scanner has two acquisition modes: the single and the coincidence modes. While the single mode is used for scanner performance evaluation and setup purposes, the coincidence acquisition mode is the standard mode used for imaging purposes [12].

Coincidence data can be acquired in list-mode or LOR-mode. Each entry of the list-mode data represents a detected event in chronological order. Time markers with high temporal resolution (at intervals of 200 μs [27]) are inserted for posterior framing. List-mode files allow flexible post-processing, which means they can be histogrammed into sinograms after the measurement and divided into predefined time frames. This framing allows the evaluation of the dynamic radiotracer distribution as a function of time. All PET data analysed in this work was recorded in list-mode.

3.2. Measurements

For this study, simultaneously acquired PET and MRI data on 12 brain tumour patients were used. All scans were carried out on the hybrid 3T MR-BrainPET. Several datasets were analysed, all of which referring to patients with histologically confirmed cerebral glioma and meningioma, some were untreated and others had undergone previous tumour resection, radiation and/or chemotherapy (or a combination thereof). Some relevant protocol details are briefly mentioned hereafter.

[2] Lutetium oxyorthosilicate.

3.2.1. PET Protocols

PET was performed using [^{18}F]-FET. For this purpose, FET at a dose of 3 MBq/kg of body weight was injected at the start of the PET acquisition. PET data was acquired for 60 min after injection in list-mode and framed into 23 time frames with variable frame length ($8 \times 5\,s,\ 2 \times 10\,s,\ 2 \times 15\,s,\ 1 \times 30\,s,\ 1 \times 60\,s,\ 1 \times 120\,s,\ 5 \times 300\,s$ and $3 \times 600\,s$). Image reconstruction was performed using the clinical standard 3D ordinary Poisson OSEM (OP-OSEM) scheme with 4 subsets and 32 iterations. The reconstructed images have $256 \times 256 \times 153$ isotropic voxels of $(1.25\ \text{mm})^3$. Once the image is reconstructed, the resulting voxel intensities were converted into activity concentrations (*e.g.* Bq/mL) instead of counts using a calibration factor. Moreover, the reconstructed images were post-filtered with a 2 mm Gaussian filter.

3.2.2. MRI Protocols

All MRI sequences were acquired simultaneous to the PET measurement. During the dynamic acquisition, a varied number of sequences can be performed, for instance, for structural and functional imaging (*e.g.* MP-RAGE[3] and EPI, respectively). Standard MRI protocols begin with a localizer sequence (2D gradient echo) recorded to check the positioning of the head, followed by a T_1-weighted MP-RAGE, which is an anatomical sequence. Other sequences composing the MR protocol are not mentioned, as they are not relevant for this study. In this context, DSC-MRI was acquired based on EPI sequence with an echo time of 32 ms and a repetition time of 1500 ms. The matrix size was 128 × 128 voxels and 20 slices with a voxel size of 1.8 × 1.8 × 5.0 mm^3 were acquired. Contrast agent[4] was injected during the EPI measurement at a dose of 0.1 mmol/kg of body weight.

[3] Magnetisation-prepared rapid acquisition with gradient echo (MP-RAGE) sequence.

[4] Dotarem® (gadoterate meglumine) – an MRI gadolinium-based contrast agent indicated for intravenous use in *e.g.* brain studies to help detecting and visualising areas with disruption of the blood brain barrier and/or abnormal vascularity.

3.3. Data Analysis

Patient motion introduces blurring in images, which is even more evident in scans with long periods of acquisition, such as the one hour dynamic [^{18}F]-FET PET scans. Furthermore, in dynamic analysis performed based on voxel intensity or ROIs, motion correction is important to avoid voxel/ROI mispositioning and therefore incorrect dynamic information. In this context, motion correction was performed using PMOD's image registration and fusion tool (PFUS). Images were motion corrected relatively to a reference image, which corresponded to an average image calculated from a range of the first frames (excluding the initial noisy frames) with negligible patient motion. Motion was visually assessed having an anatomical structure, *e.g.* nose, to determine the reference frames and the ones to be corrected.

Image registration was performed with PMOD's fusion tool as well (cross-modality rigid matching), having the anatomical MP-RAGE images as reference. Both PET and MRI images were motion corrected and co-registered following the same steps.

For the dynamic analysis, data was post-processed using MATLAB. After loading the data from both modalities, the dynamic images were filtered using a 2 mm Gaussian filter. Various width (sigma) values were tested in order to obtain better results. In general, the SNR of dynamic EPI images is relatively low, as opposed to the FET ones, which are usually very noisy. As a result, special attention was focused on the filtering of FET data to facilitate the fitting and extraction of information from the TACs.

The DSC-MRI data was converted into TCCs, $c(t)$, by using

$$c(t) = -\frac{1}{TE}\ln\left(\frac{S(t)}{S_0}\right) \tag{3.1}$$

where $S(t)$ corresponds to the MRI signal and S_0 is the prebolus baseline signal intensity, which was considered to be the first five frames of each time series [57].

The analysis was carried out on a voxel-by-voxel basis. Features from both modalities were extracted in order to produce parametric images of peak, time to peak (TTP), area under the curve (AUC) and wash-in (Figure 3.2). TTP was considered as the time from the start of the injection until maximum contrast concentration is reached; and peak was obtained from the maximum calculated for each curve. AUC was obtained calculating the integral of each curve, whilst wash-in was estimated from the maximum slope of the curve.

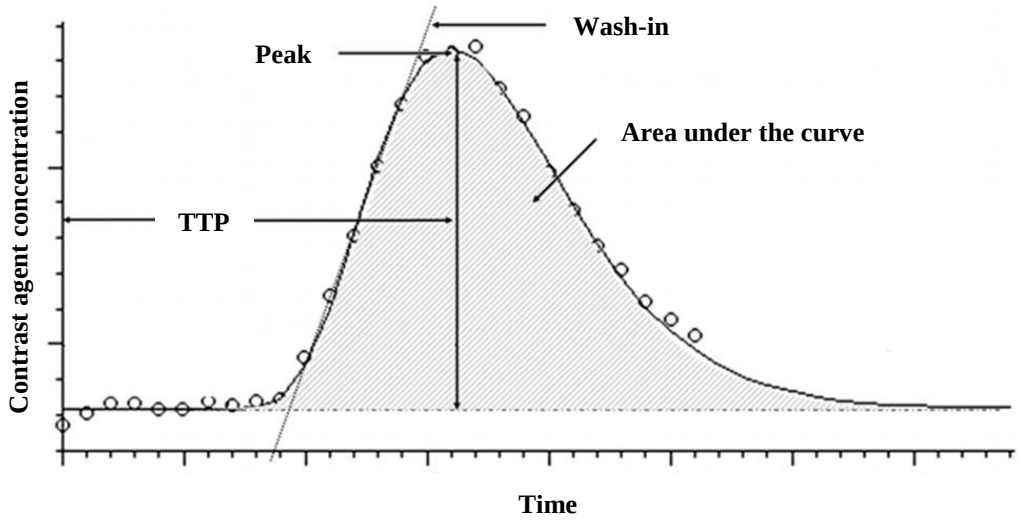

Figure 3.2. Graph illustrating a contrast time curve plotted from a normal brain tissue. Parametric images are obtained from the extracted features, such as peak, TTP, AUC, and wash-in, represented in this curve. Adapted from [58].

The correct fitting of the data is important, as the extraction of some features can be affected by the function that is adjusted to the contrast-time curves. Consequently, the fitting applied to the curves was performed using the GV function (Section 2.4.2.2.). To solve this function by running a least-squares estimation algorithm, initial coefficient values are required, *i.e.* initial guess values of the dependent variables A, α, β and t_0. It is important to note that poor starting values can lead to a solution with large residual error, as verified in the resulting simulations. While running the first fits, the initial guess values were manually adjusted to the curves. The fitted curves were visually checked to guarantee reasonable fits. Although the adjustment was only applied to a single exemplary curve for each dataset (and then run for the remaining curves), the process was neither efficient, nor prompt when analysing several datasets. Therefore, the estimation of the initial guesses of the four variables was simplified by extracting information from each curve. In this way the maximum of the curve and the time to peak were used to aid the determination of the initial guess of A and t_0, respectively. A was set to the value of the maximum (y_{max}) multiplied by a scaling factor to adjust to the curve (*i.e.* a scalar manually adjusted for the curve). The parameter t_0 was set to the value of the onset of the bolus, which was determined by searching from the time point

of the maximum (t_{max}) back to the origin looking for two successive values lying under a threshold of 10% of the maximum, as suggested by Benner *et al.* [59].

At last, the simplified formulation of the GV function derived by Madsen [52] was applied, enabling one to obtain the four initial guess values required to run the least-squares algorithm, mentioned hereafter as the *automated* method. The only estimates required are t_0 (the onset of the bolus, which can be simplified by assuming $t_0 = 0$), t_{max} and y_{max}, all of which can be estimated with the derived expressions by Madsen [52]. Further information on the mentioned simplified formulation of the GV function can be found in the Appendix.

While doing the GV curve fitting of the data, a parameter variation analysis was done in order to better understand the changes in the shape and fit of the curves, *i.e.* a variation in each GV parameter was analysed (keeping the remaining constant). Additionally, an AIF fitting analysis testing the manual and automated fitting methods was done, with the AIFs extracted with the Stroketool software.

4. Results and Discussion

As already mentioned, the broad outline of this project was to generate parametric images from dynamic MR-PET data and compare the extracted information from both modalities. Therefore, this chapter is organised as a sequence of results through the analysis course. Firstly, some data filtering results are shown. The analyses regarding the GV fitting model are presented afterwards. FET-PET and MRI curves and the resulting fitted ones are exemplified. As a consequence of these last results, a parameter variation analysis (of the GV function) was performed in order to better understand the behaviour of the fitted curves when varying the GVs. Furthermore, an AIF fitting analysis is presented, in which different fitting methods were tested. At last, some analysed datasets and their corresponding extracted parametric images are presented.

4.1. Data Filtering

As already mentioned, FET data is highly influenced by the noise, requiring appropriate data correction methods and reconstruction algorithms and also suitable filtering methods. In this context, a Gaussian filter using different width values (Figure 4.1) was tested. The resulting images led to the selection of the 2 mm as the

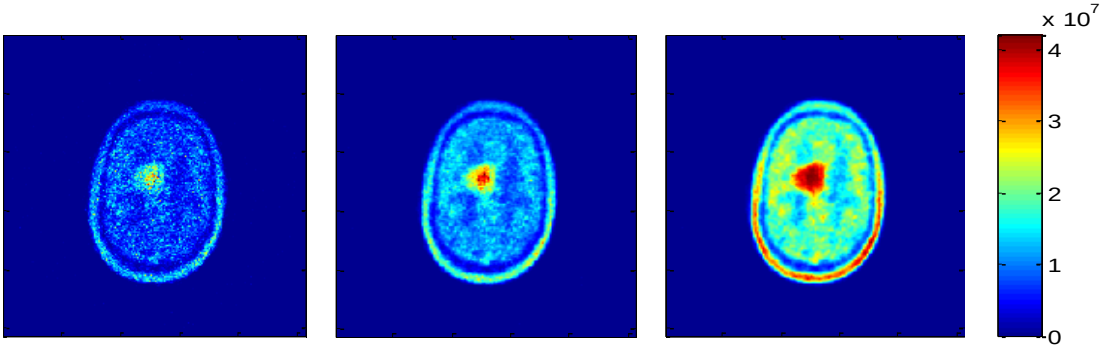

Figure 4.1. Images extracted from the FET data: an example of unfiltered image (left) and the corresponding filtered ones with 2 mm (middle) and 3 mm width (right).

filter width to apply to the reconstructed data. Also, the Gaussian filter implemented by the PMOD software was tested, although all images were processed using MATLAB, it was useful in the motion correction step (to aid in the detection of movement). Once again, the selected filter, with which better results were achieved, was the 2 mm one, as showed in Figure 4.2.

A different approach in the filtering process may be beneficial and help to obtain less noisy TACs that are more easily described and fitted by a known mathematical function. Thus enabling one to produce more accurate parametric images, as the adopted methods might have somehow limited the results.

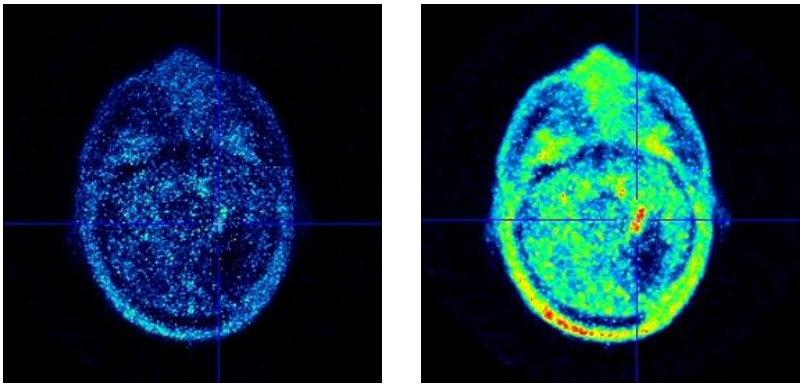

Figure 4.2. An FET-PET image filtered using the PMOD software (2 mm filter).

4.2. Gamma-variate Fitting

For the voxel-by-voxel analysis, the TCCs obtained are exemplified in Figure 4.3 and Figure 4.4. In these figures, the resulting GV fitted curves are also shown. For the EPI curves (Figure 4.3), a good fit of the observed data was achieved. However, for the TACs extracted from FET data (Figure 4.4), it was not possible to apply a fit to all image voxels. The main reason for these findings is probably due to the noisy nature of the FET curves. While in the MR data, even though there are some voxels in which it is not possible to properly fit the data, a GV function can be applied to the majority of the TCCs.

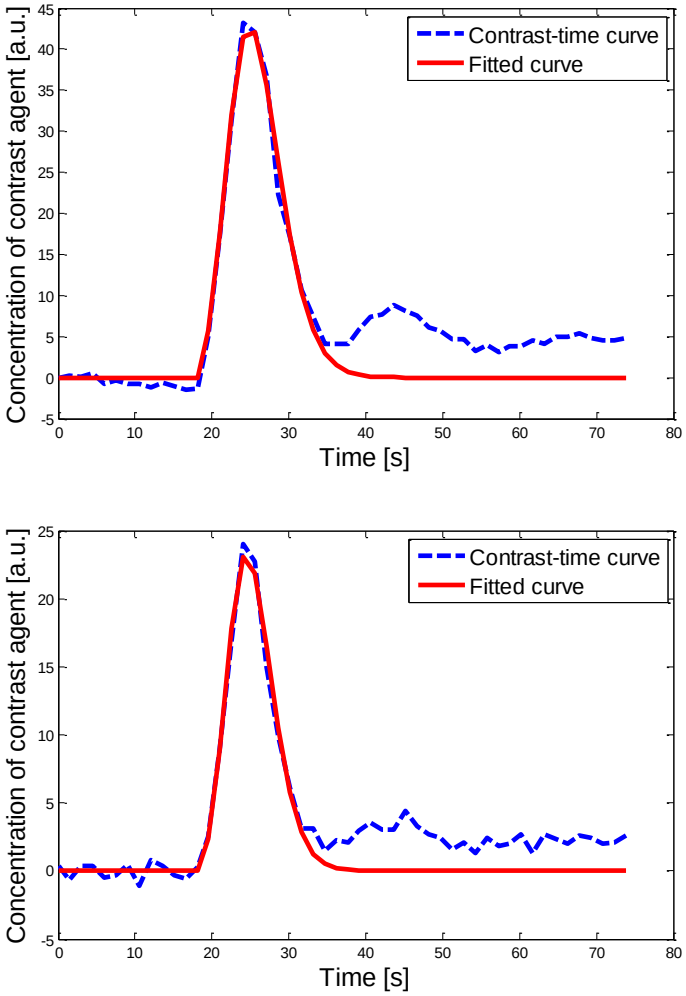

Figure 4.3. EPI contrast-time curves from a single voxel analysis and the corresponding adjusted GV function.

The fitted GV parameters were estimated having the automated method suggested by Madsen [52] as starting point. It was not possible to establish a relation between the estimated GV parameters that better fitted the curves, *i.e.* the parameters (A, α, β and t_0) obtained for one curve did not resemble the values of other curves even within the same subject. For instance, changes in α and β were found to affect both the location and magnitude of the function's maximum, and also the rise and fall times of the function, as illustrated in Figure 4.5. In fact, both variations (in α and β) were found to be very similar when merging the plots in Figure 4.5 together.

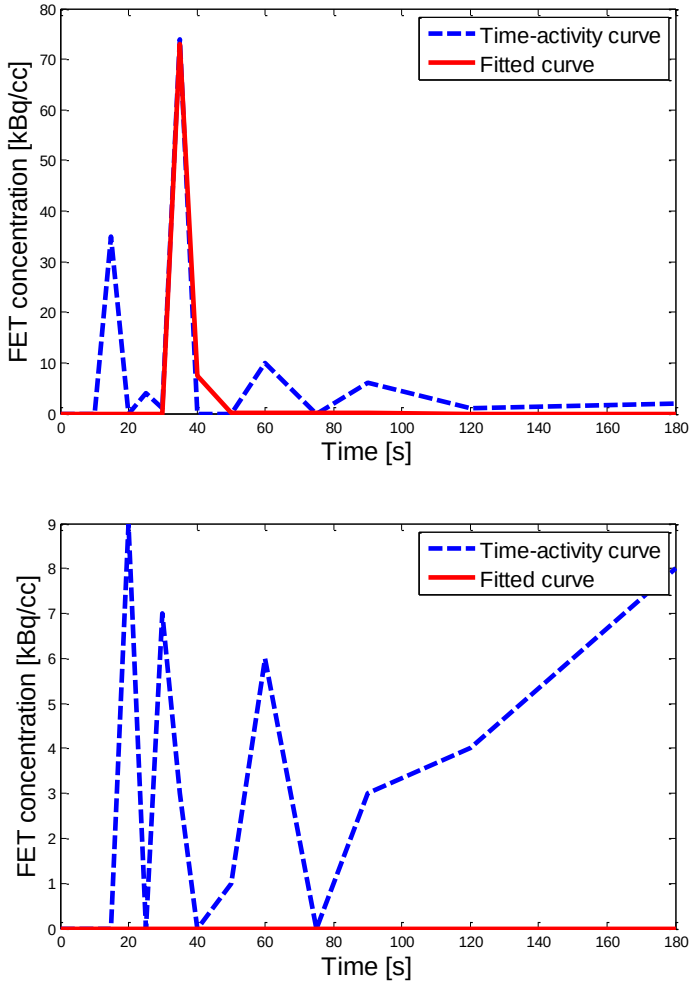

Figure 4.4. FET-PET time-activity curves from a single voxel analysis and the corresponding adjusted GV function. The levels of noise observed in the FET-derived curves hampered the fitting process, and in some cases have made it unsuccessful.

In the same line of analysis, changes in A and t_0, as described in literature, only produce effects in the magnitude and onset of the peak (Figure 4.6), respectively, without changing its shape.

Another finding while doing this parameter variation analysis was that different sets of GV parameter values can produce similar curves. Figure 4.7 illustrates an AIF (dashed line) and two different fitted curves, one of them (red line) representing the adjusted curve with initial guess values: α and β fixed at 3 and 1.5 s, respectively, which are reference values used in AIF simulations (representative of typical data in adults) as reported in [46, 45]; while A and t_0 were manually adjusted for each

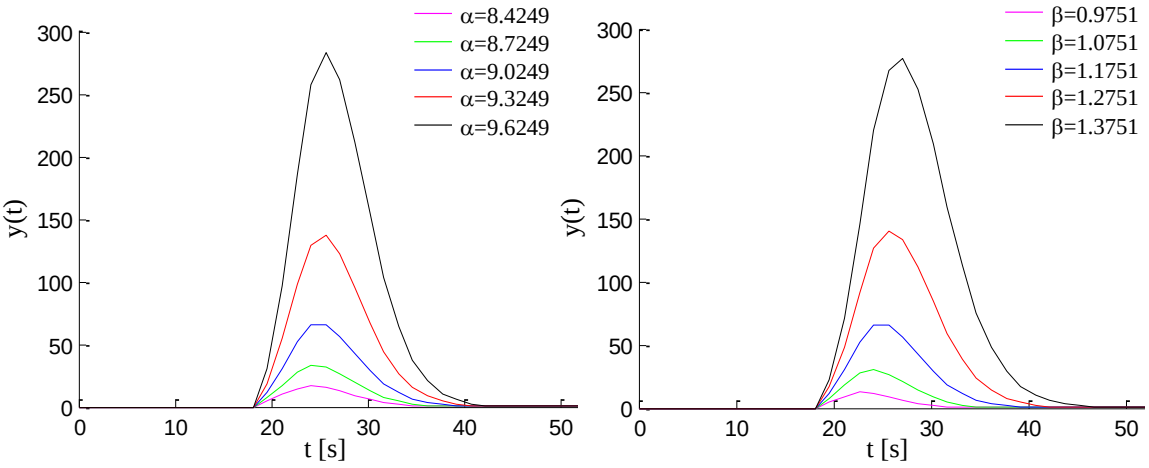

Figure 4.5. Plots of the GV function showing the differences in the location and magnitude of the curves when varying $\boldsymbol{\alpha}$ (plots on the left) and $\boldsymbol{\beta}$ (plots on the right) and keeping the remaining parameters constant. Also the rise and fall times are affected with these changes.

curve. The parameters for the other fitted curve (black line) were set with the initial values given by the automated method (*i.e.* following the simplified formulation of the GV function). Clearly the fitted curves differ in shape, but there are some similarities between them and are both considered acceptable fits of the AIF, yet the values of the estimated GVs are different.

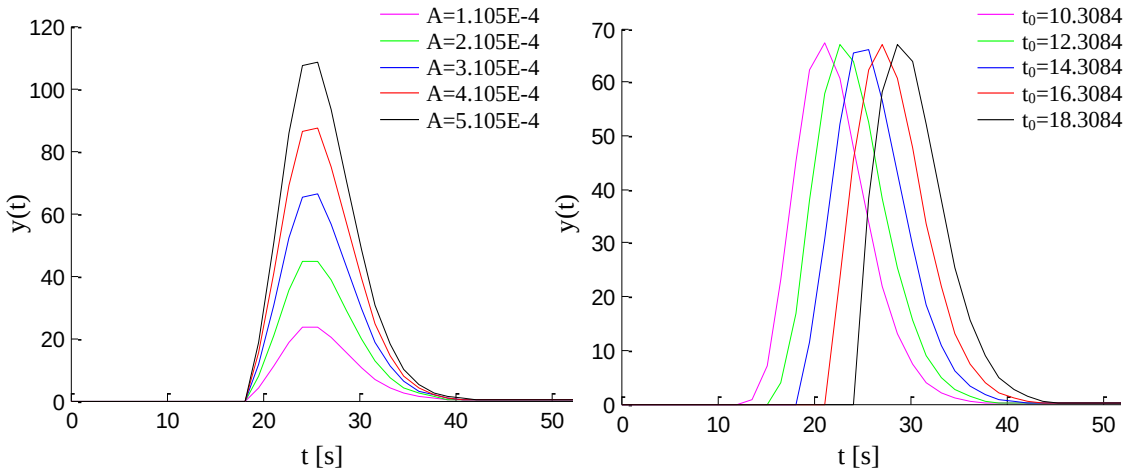

Figure 4.6. Plots of the GV function showing the differences in the amplitude and onset of the curves when varying $\boldsymbol{A}$ (plots on the left) and $\boldsymbol{t_0}$ (plots on the right), respectively, and keeping the remaining parameters constant. As expected, no changes in the shape of the curves were observed.

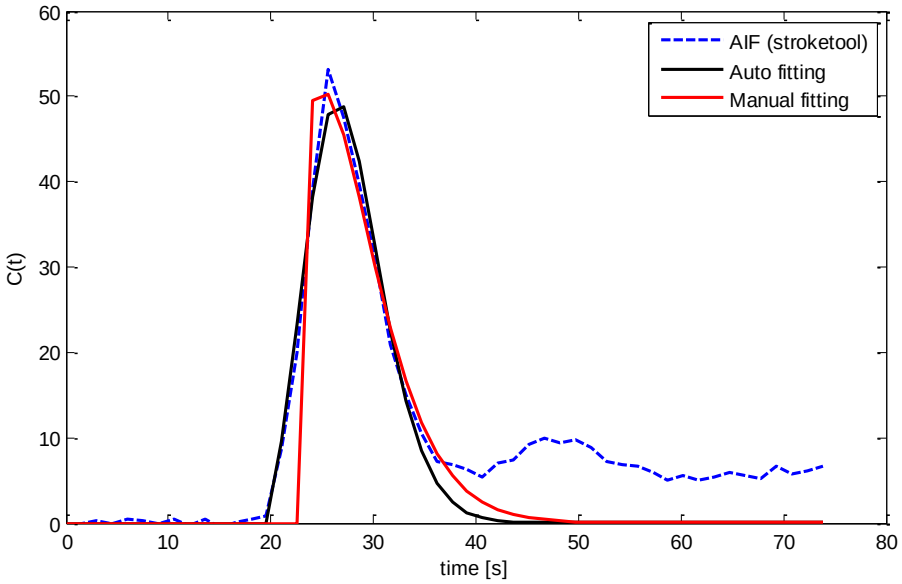

Figure 4.7. Plots of an AIF (dashed line) and its fitted curves obtained from the automated (black line) and manual methods (red line). Better results were verified with the automated fitting model.

4.2.1. AIF Fitting Analysis

This parameter variation analysis resulted from an AIF fitting analysis, in which a set of AIFs extracted with the Stroketool software from various patient data was analysed and both manual and automated fitting methods tested. Illustrative plots are showed in Figure 4.7. As expected, more accurate fits were obtained using the latter method, *i.e.* lower mean squared error (MSE) values were registered. The parameter values of the manual fitting, particularly the obtained α and β mean values, 2.5±0.6 and 2.9±0.5 respectively, differed from the literature ones previously mentioned ($\alpha = 3$ and $\beta = 1.5$). When analysing Table 4.1 with the GV parameters of the two fitting methods,

Table 4.1. AIF fitting analysis. Mean and standard deviation values of the estimated GV parameters obtained with the manual and automated fitting methods, for a set of 10 AIFs.

GV parameters	Manual fitting		Automated fitting	
	$\bar{x}$	σ	$\bar{x}$	σ
A	10,5	11,8	0,0003	0,0006
α	2,5	0,6	9,0	3,2
β	2,9	0,5	1,2	0,2
t_0	17,0	1,4	14,3	1,0

it was not possible to establish a relation between the results either from one method or the other. Particularly when analysing the automated fitting, where the values of A and α presented high standard deviation values.

4.3. Parametric Images

Results from two of the analysed datasets are presented in Figure 4.8. This figure shows the MR images from the MP-RAGE and EPI sequences (Figure 4.8a and b from each dataset (i and ii), respectively), and the corresponding extracted parametric

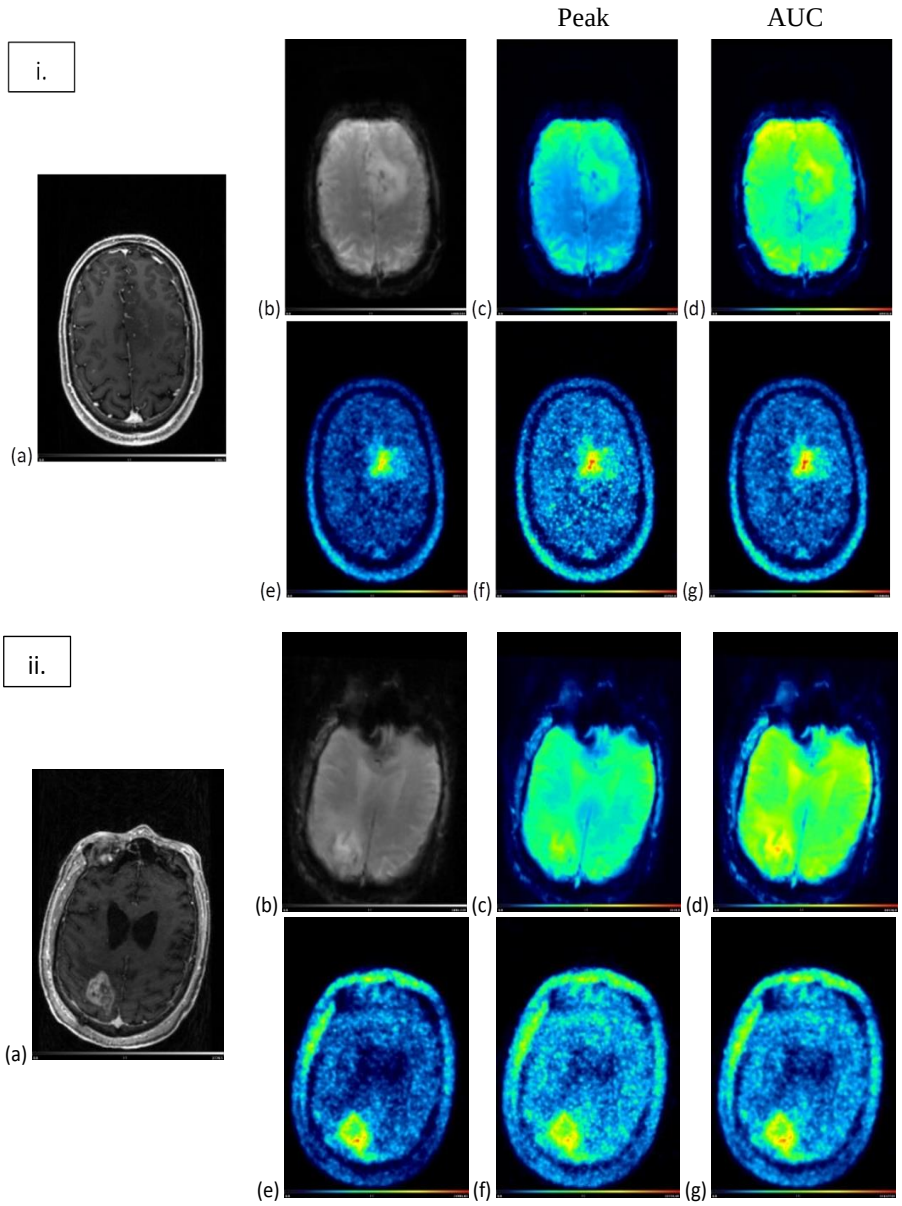

Figure 4.8. Two analysed datasets (i and ii). MRI images: MP-RAGE (post contrast) (a), EPI (b), and the corresponding extracted parametric images: peak (c) and AUC (d). FET-PET image (summed image of 20-40 min p.i.) (e) and the corresponding extracted parametric images of peak (f) and AUC (g).

images (Figure 4.8c and d). FET-PET images and its corresponding parametric images are also presented (Figure 4.8e - g). In the FET-PET parametric images (Figure 4.8f and g) an uptake area can be identified in the region of morphological changes in anatomical MR, which corresponds to the tumour region. In general, all the parametric images show gross alterations in the tumour areas (Figure 4.8c and f, and d and g from each dataset). The extracted parametric images from the dynamic PET and MR showed a good spatial registration, however the patterns are different. These results suggest that dynamic MR and PET may have extra information and that the combination of simultaneous acquisition and analysis may be beneficial.

The correct fitting of the data is important, as the extraction of the features can be affected by the function that is adjusted to the contrast-time curves. Figure 4.8 only contemplates the parametric images of peak and AUC. As already mentioned, for the FET TACs (Figure 4.4), no fitting was able to be applied to all image voxels. Due to these results, only TTP and wash-in derived from MR images were obtained (Figure 4.9). The patterns found in the peak and AUC images are not identified in the TTP and wash-in ones, namely the uptake area identified in the region of morphological changes

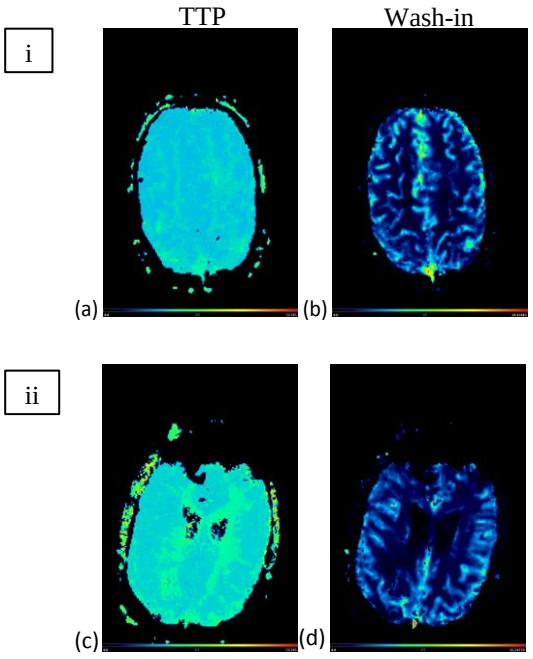

Figure 4.9. From the same analysed datasets (i and ii from Figure 4.8), parametric images of TTP ((a) and (c)) and wash-in ((b) and (d)) extracted from the EPI data.

in anatomical MR, which might indicate that different data analysis approaches are required in order to obtain all parametric images (especially TTP images from FET data, which are particularly interesting and useful in clinical routine).

5. General Discussion and Conclusions

The limitations regarding the high noise level of PET data have confirmed one of this technique's drawbacks. Even with the data smoothing and all the pre-processing corrections, PET images noisy nature plays a major role on the analysis and extraction of parametric images. As a consequence for the analysis exposed in this work, the purpose of obtaining parametric images from dynamic MR-PET data and the combination of information from both modalities has been limited for this reason. So, on the one hand there is this issue which has revealed to be a limitation in achieving all project goals. On the other hand, the choice of the fitting model to apply to the data might not have been the most appropriate one.

One thing is certain, and was the reason that supported its choice, the GV function remains the most commonly used model for hemodynamic studies. However, it presents several drawbacks which still remain a matter of controversy. Madsen [52] reported that changes in the α and β parameters affect not only the location and magnitude of the peak but also its rise and fall times, leading to uncertainty in the fitting optimisation process. In fact, this has revealed to be a challenge, mostly while adjusting the initial gamma-variates for the manual fitting of the TACs, since the slightest change in one of these parameters would produce modifications in the curves shape. Benner *et al.* [59] suggested that the GV fitting is only reliable when time resolution, maximal signal drop and SNR are kept within reasonable limits and when the initial guess values set for the least-squares estimation algorithm are ensured to be also reliable, otherwise leading to unsatisfying results. Furthermore, Li *et al.* [60] reported that the parameter A is nonlinear and thus needs to be taken into account during the fitting process in order to obtain unbiased results, as already stated by Thompson *et al.* [50].

Some other more complex models have been proposed [61, 62, 63]. For instance, Enmi *et al.* [63] developed an alternative technique for reconstructing AIFs from TCCs

of multiple brain regions (as opposed to the usual AIFs obtained from TCCs of a cerebral artery), by using a multi-exponential function.

Other approaches might have been beneficial, such as a regional analysis, instead of a voxel-by-voxel analysis, considering only the average concentration curves within a certain neighbourhood (*i.e.* within homogeneous structures). This analysis would allow to process data with better statistics, as well as reduced computing times. Or even an analysis considering only the area of morphological changes in anatomical MR (*i.e.* the tumour region). However, the achievement of parametric images revealing detailed information on every voxel would not be possible with this approach.

Also, an alternative may pass by testing the GV function and other fitting models for different curves, adding different levels of noise, and varying the model parameters so that better knowledge on the curves behaviour is achieved. By quantifying the noise level and testing which model better fits the data, this approach might be useful when next applying the model to the FET data.

Overall, the underlying purpose of developing an image analysis tool that can be used to generate parametric images from different features extracted from dynamic MR-PET data was partially achieved. The combination and subsequent comparison between the extracted information from both modalities were not possible, due to the lack of results from the dynamic PET data. Nevertheless, some parametric images were obtained and may be useful to provide extra information in tumour assessment.

Bibliography

[1] G. Hevesy. The Absorption and Translocation of Lead by Plants, *Biochem. J.*, vol. 17, pp. 439–445, 1923.

[2] M. N. Wernick and J. N. Aarsvold. *Emission Tomography: The Fundamentals of PET and SPECT*. Elsevier Academic Press, 2004.

[3] D. L. Bailey, D. W. Townsend, P. E. Valk, and M. N. Maisey. *Positron Emission Tomography: Basic Sciences*. Springer, 2005.

[4] S. R. Cherry, J. Sorenson, and M. E. Phelps. *Physics in Nuclear Medicine*, 4th ed. Elsevier Inc., 2012.

[5] N. Tsoulfanidis. *Measurement and Detection of Radiation*, 2nd ed. Taylor & Francis, 1995.

[6] M. E. Phelps. *PET: Physics, Instrumentation, and Scanners*. Springer, 2006.

[7] C. Weirich. *Quantitative PET Imaging with Hybrid MR-PET Scanners*, PhD thesis. RWTH Aachen University, 2014.

[8] C. Watson, D. Newport, and M. Casey. A single scatter simulation technique for scatter correction in 3D PET, *Three-Dimensional Image Reconstr. Radiat. Nucl. Med.*, pp. 255–268, 1996.

[9] C. C. Watson. New, faster, image-based scatter correction for 3D PET, *IEEE Trans. Nucl. Sci.*, vol. 47, no. 4, pp. 1587–1594, 2000.

[10] J. Carney, D. Townsend, V. Rappoport, and B. Bendriem. Method for transforming CT images for attenuation correction in PET/CT imaging, *Med. Phys.*, vol. 33, no. 4, pp. 976–983, 2006.

[11] E. Rota Kops and H. Herzog. Template based attenuation correction for PET in MR-PET scanners, *2008 IEEE Nucl. Sci. Symp. Conf. Rec.*, pp. 3786–3789, 2008.

[12] M. Gaens. *Analysis, Characterisation and Setup of a Block Detector Used in a 3TMR-BrainPET System*, diploma thesis. Technische Universitat Dortmund, 2010.

[13] D. Brasse, P. E. Kinahan, C. Lartizien, C. Comtat, M. Casey, and C. Michel. Correction methods for random coincidences in fully 3D whole-body PET: impact on data and image quality, *J. Nucl. Med.*, vol. 46, no. 5, pp. 859–67, 2005.

[14] T. R. Oakes, V. Sossi, and T. J. Ruth. Normalization for 3D PET with a low-scatter planar source and measured geometric factors, *Phys. Med. Biol.*, vol. 43, no. 4, pp. 961–972, 1998.

[15] S. Yamamoto, M. Amano, S. Miura, H. Iida, and I. Kanno. Deadtime correction method using random coincidence for PET, *J. Nucl. Med.*, vol. 27, no. 12, pp. 1925–1928, 1986.

[16] M. E. Daube-Witherspoon and R. E. Carson. Unified deadtime correction model for PET, *IEEE Trans. Med. Imaging*, vol. 10, no. 3, pp. 267–275, 1991.

[17] F. H. Fahey. Data acquisition in PET imaging, *J. Nucl. Med. Technol.*, vol. 30, no. 2, pp. 39–49, 2002.

[18] H. Zaidi. *Quantitative Analysis in Nuclear Medicine Imaging*. Springer, 2006.

[19] L. A. Shepp and Y. Vardi. Maximum Likelihood Reconstruction for Emission Tomography, *IEEE Trans. Med. Imaging*, vol. 1, no. 2, pp. 113–122, 1982.

[20] H. M. Hudson and R. S. Larkin. Accelerated image reconstruction using ordered subsets of projection data, *IEEE Trans. Med. Imaging*, vol. 13, no. 4, pp. 601–609, 1994.

[21] D. G. Nishimura. *Principles of Magnetic Resonance Imaging*. Department of Electrical Engineering, Stanford University, 1996.

[22] M. A. Brown and R. C. Semelka. *MRI: Basic principles and applications*, 3rd ed. John Wiley & Sons, Inc., 2003.

[23] D. Weishaupt, V. D. Köchli, and B. Marincek. *How Does MRI Work? An Introduction to the Physics and Function of Magnetic Resonance Imaging*, 2nd ed. Springer. Berlin, Heidelberg, 2006.

[24] P. Suetens. *Fundamentals of Medical Imaging*, 2nd ed. Cambridge University Press, 2009.

[25] R. L. DeLaPaz. Echo-planar imaging, *Radiographics*, vol. 14, no. 5, pp. 1045 –1058, 1994.

[26] T. Beyer, D. Townsend, and T. Brun. A combined PET/CT scanner for clinical oncology, *J. Nucl. Med.*, vol. 41, pp. 1369–1379, 2000.

[27] H. Herzog, K.-J. Langen, C. Weirich, E. Rota Kops, J. Kaffanke, L. Tellmann, J. Scheins, I. Neuner, G. Stoffels, K. Fischer, L. Caldeira, H. H. Coenen, and N. J. Shah. High resolution BrainPET combined with simultaneous MRI, *Nuklearmedizin*, vol. 50, no. 2, pp. 74–82, 2011.

[28] H. Herzog and J. van den Hoff. Combined PET/MR systems: an overview and comparison of currently available options, *Q J Nucl Med Mol Imaging*, vol. 56, no. 3, pp. 247–267, 2012.

[29] J. Scheins, M. Ullisch, L. Tellmann, C. Weirich, E. Rota Kops, H. Herzog, and N. J. Shah. PET motion correction in LOR space using scanner-independent, adaptive projection data for image reconstruction with PRESTO, *Nucl. Sci. Symp. Med. Imaging Conf.*, pp. 4099–4101, 2011.

[30] H. Zaidi and A. Del Guerra. An outlook on future design of hybrid PET/MRI systems, Med. Phys., vol. 38, no. 10, pp. 5667–5689, 2011.

[31] M. Hofmann, B. Pichler, B. Scholkopf, and T. Beyer. Towards quantitative PET/MRI: a review of MR-based attenuation correction techniques, *Eur. J. Nucl. Med. Mol. Imaging*, vol. 36, pp. 93–104, 2009.

[32] R. Grazioso, R. Ladebeck, M. Schmand, and R. Krieg. APD-based PET for combined MR-PET imaging Detector, *Proc. ISMRM 13th Sci. Meet.*, 2005.

[33] H.-P. W. Schlemmer, B. J. Pichler, M. Schmand, Z. Burbar, C. Michel, R. Ladebeck, K. Jattke, D. Townsend, C. Nahmias, P. K. Jacob, W.-D. Heiss, and C. D. Claussen. Simultaneous MR/PET imaging of the human brain: feasibility study, *Radiology*, vol. 248, no. 3, pp. 1028–1035, 2008.

[34] A. J. Reader, F. Sureau, C. Comtat, R. Trébossen, and I. Buvat. Simultaneous estimation of temporal basis functions and fully 4D PET images, *Phys. Med. Biol.*, vol. 51, pp. 5455–5474, 2006.

[35] R. Carson, M. Daube-Witherspoon, and P. Herscovitch. *Quantitative Functional Brain Imaging with Positron Emission Tomography*, Elsevier Academic Press, 1998.

[36] G. Pöpperl, F. W. Kreth, J. Herms, W. Koch, J. H. Mehrkens, F. J. Gildehaus, H. a Kretzschmar, J. C. Tonn, and K. Tatsch. Analysis of ^{18}F-FET PET for grading of recurrent gliomas: is evaluation of uptake kinetics superior to standard methods?, *J. Nucl. Med.*, vol. 47, no. 3, pp. 393–403, 2006.

[37] K. Langen, K. Hamacher, M. Weckesser, F. Floeth, G. Stoffels, D. Bauer, H. Coenen, and D. Pauleit. O-(2-[^{18}F]fluoroethyl)-L-tyrosine: uptake mechanisms and clinical applications, *Nucl Med Bio*, vol. 33, no. 3, pp. 287–294, 2006.

[38] C. Kratochwil, S. E. Combs, K. Leotta, A. Afshar-Oromieh, S. Rieken, J. Debus, U. Haberkorn, and F. L. Giesel. Intra-individual comparison of ^{18}F-FET and ^{18}F-DOPA in PET imaging of recurrent brain tumors, *Neuro. Oncol.*, vol. 16, no. 3, pp. 434–440, 2014.

[39] D. Pauleit, A. Zimmermann, G. Stoffels, D. Bauer, M. O. Flu, K. Hamacher, H. H. Coenen, and K. Langen. PET Compared with ^{18}F-FDG PET and CT in Patients with Head and Neck Cancer, *J. Nucl. Med.*, vol. 47, no. 2, pp. 256–261, 2006.

[40] P. Heiss, S. Mayer, M. Herz, H. J. Wester, M. Schwaiger, and R. Senekowitsch-Schmidtke. Investigation of transport mechanism and uptake kinetics of O-(2-[^{18}F]fluoroethyl)-L-tyrosine in vitro and in vivo, *J. Nucl. Med.*, vol. 40, no. 8, pp. 1367–1373, 1999.

[41] M. K. Nedergaard, K. Kristoffersen, S. R. Michaelsen, J. Madsen, H. S. Poulsen, M. T. Stockhausen, U. Lassen, and A. Kjaer. The use of longitudinal ^{18}F-FET MicroPET imaging to evaluate response to irinotecan in orthotopic human glioblastoma multiforme xenografts, *PLoS One*, vol. 9, no. 6, p. e100009, 2014.

[42] N. L. Jansen, B. Suchorska, V. Wenter, S. Eigenbrod, C. Schmid-Tannwald, A. Zwergal, M. Niyazi, M. Drexler, P. Bartenstein, O. Schnell, J.-C. Tonn, N. Thon, F.-W. Kreth, and C. la Fougere. Dynamic ^{18}F-FET PET in Newly Diagnosed Astrocytic Low-Grade Glioma Identifies High-Risk Patients, *J. Nucl. Med.*, vol. 55, no. 2, pp. 198–203, 2014.

[43] N. Silva. *On the Use of Image Derived Input Function for Quantitative PET Imaging with a Simultaneous Measuring MR-BrainPET*, MSc thesis. Universidade de Lisboa, Faculdade de Ciências, 2012.

[44] F. Calamante. Arterial input function in perfusion MRI: A comprehensive review, *Prog. Nucl. Magn. Reson. Spectrosc.*, vol. 74, pp. 1–32, 2013.

[45] F. Calamante, D. G. Gadian, and A. Connelly. Delay and dispersion effects in dynamic susceptibility contrast MRI: simulations using singular value decomposition, *Magn. Reson. Med.*, vol. 44, no. 3, pp. 466–473, 2000.

[46] L. Østergaard, R. Weisskoff, D. Chesler, C. Gyldensted, and B. Rosen. High resolution measurement of cerebral blood flow using intravascular tracer bolus passages. Part I: Mathematical approach and statistical analysis, *Magn Reson Med*, vol. 36, no. 5, pp. 715–725, 1996.

[47] H. Herzog, K.-J. Langen, J. Kaffanke, C. Weirich, I. Neuner, G. Stoffels, E. R. Kops, J. Scheins, L. Tellmann, and N. J. Shah. MR-PET opens new horizons in neuroimaging, *Future Neurol.*, vol. 5, no. 6, pp. 807–815, 2010.

[48] T. Ishiguchi and S. Takahashi. Safety of gadoterate meglumine (Gd-DOTA) as a contrast agent for magnetic resonance imaging: results of a post-

marketing surveillance study in Japan, *Drugs R. D.*, vol. 10, no. 3, pp. 133–45, 2010.

[49] N. D. Forkert, J. Fiehler, T. Ries, T. Illies, D. Möller, H. Handels, and D. Säring. Reference-based linear curve fitting for bolus arrival time estimation in 4D MRA and MR perfusion-weighted image sequences, *Magn. Reson. Med.*, vol. 65, no. 1, pp. 289–294, 2011.

[50] H. K. Thompson, C. F. Starmer, R. E. Whalen, and H. D. McIntosh. Indicator Transit Time Considered as a Gamma Variate, *Circ. Res.*, vol. 14, no. 6, pp. 502–515, Jun. 1964.

[51] R. Davenport. The Derivation of the Gamma-Variate Relationship for Tracer Dilution Curves, *J. Nucl. Med.*, vol. 24, pp. 945–948, 1983.

[52] M. T. Madsen. A simplified formulation of the gamma variate function, *Phys. Med. Biol.*, vol. 37, no. 7, pp. 1597–1600, 1992.

[53] H. Kelbaek, O. J. Hartling, K. Skagen, O. Munck, O. Henriksen, and J. Godtfredsen. First-pass radionuclide determination of cardiac output: An improved gamma camera method, *J. Nucl. Med.*, vol. 28, no. 8, pp. 1330–1334, 1987.

[54] D. L. Maltz and S. Treves. Quantitative radionuclide angiocardiography: Determination of Qp:Qs in children, *Circulation*, vol. 47, no. 5, pp. 1049–56, 1973.

[55] E. Evans, S. J. Sawiak, A. O. Ward, G. Buonincontri, R. C. Hawkes, and T. Adrian Carpenter. Comparison of first pass bolus AIFs extracted from sequential ^{18}F-FDG PET and DSC-MRI of mice, *Nucl. Instruments Methods Phys. Res. Sect. A Accel. Spectrometers, Detect. Assoc. Equip.*, vol. 734, no. PART B, pp. 137–140, 2014.

[56] H. Herzog. PET/MRI: Challenges, solutions and perspectives, *Z. Med. Phys.*, vol. 22, no. 4, pp. 281–298, 2012.

[57] E. S. Paulson and K. M. Schmainda. Comparison of Dynamic Susceptibility-weighted Contrast-enhanced MR Methods: Recommendations for Measuring Relative Cerebral Blood Volume in Brain Tumors, *Radiology*, vol. 249, no. 2, pp. 601–613, 2008.

[58] B. F. Tomandl, E. Klotz, D. Phys, R. Handschu, B. Stemper, F. Reinhardt, W. J. Huk, K. E. Eberhardt, and S. Fateh-moghadam. Comprehensive Imaging of Ischemic Stroke with Multisection CT, *RadioGraphics*, vol. 23, no. 3, pp. 565–592, 2003.

[59] T. Benner, S. Heiland, G. Erb, M. Forsting, and K. Sartor. Accuracy of gamma-variate fits to concentration-time curves from dynamic susceptibility-contrast enhanced MRI: influence of time resolution, maximal

signal drop and signal-to-noise, *Magn Reson Imaging*, vol. 15, no. 3, pp. 307–317, 1997.

[60] X. Li, J. Tian, and R. K. Millard. Erroneous and inappropriate use of gamma fits to tracer-dilution curves in magnetic resonance imaging and nuclear medicine, *Magn. Reson. Imaging*, vol. 21, no. 9, pp. 1095–1096, 2003.

[61] M. J. P. Van Osch, E. J. P. A. Vonken, O. Wu, M. A. Viergever, J. Van der Grond, and C. J. G. Bakker. Model of the human vasculature for studying the influence of contrast injection speed on cerebral perfusion MRI, *Magn. Reson. Med.*, vol. 50, no. 3, pp. 614–622, 2003.

[62] J. Bredno, M. E. Olszewski, and M. Wintermark. Simulation model for contrast agent dynamics in brain perfusion scans, *Magn. Reson. Med.*, vol. 64, no. 1, pp. 280–290, 2010.

[63] J. Enmi, N. Kudomi, T. Hayashi, A. Yamamoto, S. Iguchi, T. Moriguchi, Y. Hori, K. Koshino, T. Zeniya, N. J. Shah, N. Yamada, and H. Iida. Quantitative assessment of regional cerebral blood flow by dynamic susceptibility contrast-enhanced MRI, without the need for arterial blood signals, *Phys. Med. Biol.*, vol. 57, no. 23, pp. 7873–7892, 2012.

Appendix

Gamma-variate Function

The simplified formulation of the GV function proposed by Madsen [52], which was applied in the estimation of the curves to fit the real data, begins with the GV in its usual form:

$$y(t) = A(t - t_0)^{\alpha} e^{-(t-t_0)/\beta}, \quad t > t_0. \tag{A.1}$$

Because the origin can be arbitrarily selected, (A.1) can be simplified by assuming $t_0 = 0$:

$$y(t) = At^{\alpha} e^{-t/\beta}. \tag{A.2}$$

The parameter β can be written in terms of α and t_{max} by taking the first derivate of (A.2) and setting it to 0:

$$\begin{aligned} y'(t_{max}) &= 0 \\ &= A{t_{max}}^{\alpha-1} e^{-t_{max}/\beta} \left(\alpha - \frac{t_{max}}{\beta}\right) \end{aligned} \tag{A.3}$$

which yields $t_{max} = \alpha \cdot \beta$ or $\beta = \frac{t_{max}}{\alpha}$. Using the last result in (A.2) one obtains:

$$y(t) = At^{\alpha} e^{-\alpha t/t_{max}}, \tag{A.4}$$

which can be rewritten in terms of y_{max}:

$$y_{max} = y(t_{max}) = A{t_{max}}^{\alpha} e^{-\alpha} \tag{A.5}$$

and, thus, yielding $A = y_{max}{t_{max}}^{-\alpha} e^{\alpha}$. Substituting this into equation (A.4) and after redefining the independent variable t in terms of t_{max}, *i.e.* by letting $t' = t/t_{max}$ (or $t' = (t - t_0)/(t_{max} - t_0)$ for $t_0 \neq 0$), the resulting simplified equation is

$$\begin{aligned} y(t') &= y_{max}{t_{max}}^{-\alpha} e^{\alpha} {t_{max}}^{\alpha} {t'}^{\alpha} e^{-\alpha t'} \\ &= y_{max} {t'}^{\alpha} e^{\alpha(1-t')}. \end{aligned} \tag{A.6}$$

Taking the natural logarithm of both sides of equation (A.6) one obtains:

$$\ln y(t') = \ln y_{max} + \alpha(1 + \ln t' - t'), \tag{A.7}$$

which has the form of a linear equation $y = C + \alpha x$, where $y = \ln y(t')$ and $x = (1 + \ln t' - t')$. (A.7) can now be solved for α (and afterwards, β and A since y_{max} and t_{max} can be estimated beforehand) by running a linear least-squares fit, *i.e.* from the linear regression of the natural logarithm of $y(t')$ with $(1 + \ln t' - t')$ as the independent variable. To note that the least-squares fitting of (A.1) is more complicated since the independent variable associated with α and β are coupled, as stated by Madsen [52].

Acronyms

AIF	Arterial input function
APD	Avalanche photodiode
AUC	Area under the curve
BAT	Bolus arrival time
CBF	Cerebral blood flow
CT	Computed tomography
DSC	Dynamic susceptibility contrast
DWI	Diffusion weighted imaging
EPI	Echo-planar imaging
[^{18}F]-FDG	[^{18}F]-fluorodeoxyglucose
[^{18}F]-FET	O-(2-[^{18}F]-fluoroethyl)-L-tyrosine
FID	Free induction decay
fMRI	Functional magnetic resonance imaging
FOV	Field of view
GE	Gradient-echo
GV	Gamma-variate
LAT	L-type amino acid transporter
LOR	Line of response
LSO	Lutetium oxyorthosilicate
MLEM	Maximum-likelihood expectation-maximisation
MP-RAGE	Magnetisation-prepared rapid acquisition with gradient echo
MRI	Magnetic resonance imaging
MSE	Mean squared error
NMR	Nuclear magnetic resonance
OP	Ordinary Poisson
OSEM	Ordered-subsets expectation-maximisation

PET	Positron emission tomography
PFUS	PMOD image registration and fusion tool
PMT	Photomultiplier tube
RF	Radio frequency
ROI	Region of interest
SE	Spin-echo
SiPM	Silicon photomultiplier
SNR	Signal-to-noise ratio
SPECT	Single photon emission computed tomography
SSS	single scatter simulation
TAC	Time-activity curves
TCC	Time-concentration curves
TE	Echo time
TR	Repetition time
TTP	Time to peak

Acknowledgements

To begin with, I would like to express my deepest gratitude to Liliana Caldeira for her permanent support, willingness to help and availability. I am also grateful to Professor Nuno Matela for his support and guidance. Without their encouragement and all their suggestions, this work would not have been possible.

I would like to thank Professor N. Jon Shah for giving me the opportunity to work at the INM-4 (Forschungszentrum Jülich). A special thanks to Nuno da Silva and Dr Christian Filβ for all the support, availability and feedback. A big thank you goes to the entire PET group (Dr. Elena Rota Kops, Michaela Gaens, Christoph Weirich, Philipp Lohmann, Jürgen Scheins, Lutz Tellmann) and many other people at the INM-4. I would also like to express my gratitude to Professor Dr. Karl-Josef Langen for the scientific support and suggestions.

I would like to mention my fellow students and friends, Danielle Baptista, Rita Gigante, Mauro Sousa, Melissa Botelho, Inês Costa, Daniela Cunha, David Soares, Tiago Martins, whom I spent so many hours with during the last years.

Finally, I am greatly thankful to my loving parents, brother and grandmother, for their tremendous support and affection, which were crucial for keeping me going forward in times of lower motivation; and also to Carolina, for her tireless help.